Computing the viscous effect in early-time drop impact dynamics

Shruti Mishra[1], Shmuel M. Rubinstein[1,2] and Chris H. Rycroft[1,3]†

[1]John A. Paulson School of Engineering and Applied Sciences, Harvard University, Cambridge, MA 02138, USA

[2]The Racah Institute of Physics, The Hebrew University of Jerusalem, Jerusalem 91904, Israel

[3]Computational Research Division, Lawrence Berkeley Laboratory, Berkeley, CA 94720, USA

The impact of a liquid drop on a solid surface involves many intertwined physical effects, and is influenced by drop velocity, surface tension, ambient pressure and liquid viscosity, among others. Experiments by Kolinski *et al.* (2014*b*) show that the liquid–air interface begins to deviate away from the solid surface even before contact. They found that the lift-off of the interface starts at a critical time that scales with the square root of the kinematic viscosity of the liquid. To understand this, we study the approach of a liquid drop towards a solid surface in the presence of an intervening gas layer. We take a numerical approach to solve the Navier–Stokes equations for the liquid, coupled to the compressible lubrication equations for the gas, in two dimensions. With this approach, we recover the experimentally captured early time effect of liquid viscosity on the drop impact, but our results show that lift-off time and liquid kinematic viscosity have a more complex dependence than the square root scaling relationship. We also predict the effect of interfacial tension at the liquid–gas interface on the drop impact, showing that it mediates the lift-off behavior.

Key words: drops, capillary flows, Navier–Stokes equations, computational methods

1. Introduction

The dynamics of a falling liquid drop as it impacts on a substrate depend on the initial conditions and physical properties of the liquid, the surrounding media and the substrate. Depending on the relevant physical parameters, the liquid drop may splash, spread or bounce upon impact with a solid substrate. The diversity of patterns produced by liquid drops impacting on a solid substrate in the presence of ambient air were first captured by Worthington (1877), even before the invention of flash photography, through observations of patterns under the light of a spark produced by a break in an electric circuit when the drop hits the substrate. Worthington's drawings of these patterns sparked many investigations into the physical phenomena associated with drop impact, many of which are summarized in review articles (Rein 1993; Yarin 2006; Josserand & Thoroddsen 2016).

Many physical parameters are known to affect the dynamics of a drop upon impact with a substrate (Rioboo *et al.* 2002). These include the initial size and

† Email address for correspondence: chr@seas.harvard.edu

velocity of the drop (Pasandideh-Fard *et al.* 1996; Riboux & Gordillo 2014), viscosity of the liquid (Pasandideh-Fard *et al.* 1996; Stevens *et al.* 2014), pressure and viscosity of the surrounding medium (Xu *et al.* 2005; Sprittles 2015), interfacial tension between the liquid and its surrounding medium (Rioboo *et al.* 2003; Pasandideh-Fard *et al.* 1996), and the physical properties of the substrate (Range & Feuillebois 1998; Rein 1993; Yarin 2006; Latka *et al.* 2012; Josserand & Thoroddsen 2016). Experiments by Xu *et al.* (2005) show that in the impact of a liquid drop on a solid substrate, ambient air pressure determines whether the drop eventually splashes, characterized by the ejection of a number of small drops into the air, or forms a thin film and spreads smoothly onto the surface (Driscoll *et al.* 2010). This suggests a role of the surrounding gaseous medium in determining the impact dynamics even before the drop makes contact with the solid substrate, motivating investigation into the role of an intervening gaseous layer in determining dynamics of a liquid drop as it approaches a solid substrate, prior to contact of the drop with the substrate.

Theoretical work on the role of an intervening layer of gas in the approach of a liquid drop towards a solid surface has been carried out in simplified two-dimensional (Mandre *et al.* 2009; Mani *et al.* 2010; Mandre & Brenner 2012; Moore *et al.* 2013) and axisymmetric (Hicks & Purvis 2010) geometries. Some of these theoretical investigations (Mandre *et al.* 2009; Mani *et al.* 2010; Hicks & Purvis 2010; Mandre & Brenner 2012) consider an inviscid liquid drop falling towards a solid surface in the presence of an ideal gas, and predict that the drop deforms due to a buildup of pressure in the gas trapped underneath the drop, prior to its contact with the solid substrate. Since these studies assume the fluid flow in the drop is inviscid, the velocity field is given by a potential flow. This substantially simplifies the analysis, allowing the dynamics to be modeled using values of relevant field variables exclusively at the liquid–gas interface using a lubrication approximation, without explicitly computing the fluid flow in the bulk of the drop. A schematic of the deformation of the drop is shown in Figures 1(a) and 1(b).

The theoretical predictions of drops deforming on a layer of air between the liquid drop and solid substrate, prior to contact between the drop and the substrate, are consistent with previous experimental observations (Thoroddsen *et al.* 2005). Measurements of the air layer thickness underneath the impacting drop have been performed (Driscoll & Nagel 2011; Kolinski *et al.* 2012; van der Veen *et al.* 2012; de Ruiter *et al.* 2012). Subsequent experimental work by Kolinski *et al.* (2014*b*) shows the effect of liquid viscosity on the evolution of the liquid–air interface even before contact with the substrate, which is not captured by the potential flow description of the evolution of liquid dynamics in previous theoretical work (Mandre *et al.* 2009; Mani *et al.* 2010; Mandre & Brenner 2012).

In this work, we are concerned with the dynamics of a liquid drop as it approaches a rigid, non-porous, solid surface, in the presence of an ambient gas. We modify the physical model of Mandre, Mani and Brenner by incorporating the viscosity of the liquid. Due to the additional viscous term in the governing equations for the liquid, the coupled interaction of the liquid and gas becomes theoretically intractable, and it is necessary to solve numerically for the fluid flow in the bulk of the drop. There are a variety of previous computational studies of drop impact, such as looking at the dynamics of spreading (Eggers *et al.* 2010), splashing (Josserand & Zaleski 2003; Boelens & de Pablo 2018), or rebound from superhydrophobic surfaces (Renardy *et al.* 2003). Duchemin & Josserand (2011) generalized the potential flow

model of Mandre *et al.* (2009) to work in axisymmetric coordinates, where the liquid–gas interface is represented as an arbitrary curve, allowing a full spherical drop to be represented. With this model, they were able to predict the emergence of a thin jet skating above the gas layer, and they found that without surface tension a finite-time singularity forms where the liquid–gas interface touches the substrate. More recently, Duchemin & Josserand (2020) solved the lubrication equations in the thin gas layer; this work describes the drainage of the gas during impact of a drop onto a solid substrate or a liquid film.

Philippi *et al.* (2016) and Jian *et al.* (2018) examined the early stages of drop impact, making use of the Gerris/Basilisk flow solvers (Popinet 2003, 2009; Lagrée *et al.* 2011; Popinet 2015) for tracking the liquid–gas interface. This simulation framework provides greater flexibility allowing the dynamics to be tracked over a longer time. In comparison, our reduced description uses a simpler description of the initial dynamics, and is well-suited to handle the disparate length scales between the gas layer and the drop. We solve the incompressible Navier–Stokes equations in the drop, using a modern implementation of Chorin's projection method (Chorin 1967, 1968) that incorporates improvements from Almgren, Bell, Collela and coworkers (Bell *et al.* 1989; Colella 1990; Almgren *et al.* 1996). Our numerical model allows us to resolve the flow field and pressure in the drop, and examine the effects of many different physical parameters in ways (e.g., viscosity, surface tension) that would be difficult to do in an experiment. We validate our model using theoretical results (Mandre *et al.* 2009; Mani *et al.* 2010; Mandre & Brenner 2012). Using our model, we are able to recapitulate the square-root scaling with liquid viscosity of the lift-off time observed by Kolinski *et al.* (2014*b*). However, our results show that the precise relationship between lift-off time and liquid viscosity is more complicated. We explore the dependence of lift-off time on surface tension, initial drop velocity, and drop radius.

In the following sections, we describe the physical model and parameter regime, followed by approximations made in the simulation domain. We then describe the results from our simulations, along with comparisons with previous theoretical and experimental studies. Our numerical results are consistent with theoretical calculations (Mandre *et al.* 2009) as well as experimental results (Kolinski *et al.* 2014*b*). Our results predict the effect of viscosity and interfacial tension on the dynamics of drop impact.

2. Model

In this section, we first explain the physical set-up and specify the parameter regime considered in the rest of this work. Based on the physical set-up and parameter regime, we then describe the mathematical model. The mathematical model largely derives from the previous theoretical work of Mandre et al. (Mandre *et al.* 2009; Mani *et al.* 2010; Mandre & Brenner 2012). We specify the predictions made by this model, experimentally-observed deviations from these predictions, and then the mathematical model used in our work. We then use this mathematical model to derive appropriate boundary conditions for the flow in the drop.

2.1. *Physical problem and parameter regime*

The physical set-up is a drop of liquid falling towards a flat, solid surface in the presence of a surrounding gas. As the liquid drop falls towards the solid surface, it interacts with the surrounding gas. We are interested in modeling and simulating

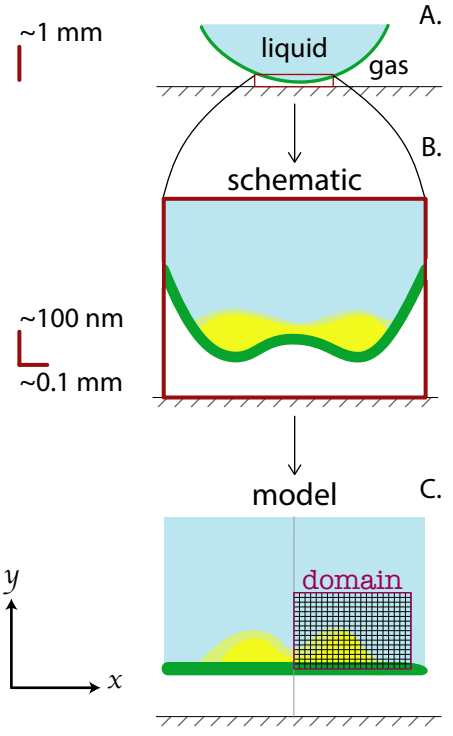

Figure 1: Schematic of the physical and computational model. (a) Relative locations of the falling drop, intervening gas layer and solid substrate. (b) A schematic zoomed into the region of interest, showing an exaggerated view of a deformed liquid–gas interface (green), and a schematic of the region where viscous effects are important (yellow). (c) Control volume and grid for discretization constructed in the fluid domain.

the coupled dynamics of the liquid and the gas before the liquid makes contact with the solid surface.

Figure 1(a) shows a schematic of the physical problem, indicating the relative locations of the liquid drop, the surrounding gas and the solid surface. The drop is initially spherical, with radius R, falling towards a horizontal solid surface at uniform vertical velocity V_0. The gas is initially at uniform pressure P_0. We specify the values of initial conditions and physical properties considered for the liquid and air in Table 1. We use the subscripts l and g to denote the liquid drop and the gas, respectively, and 0 to denote the initial conditions.

In the parameter regime specified in Table 1 potential flow theory argues that the relevant Reynolds number, based on the initial velocity V_0 and drop radius R, is $\mathcal{O}(10^2)$, allowing for an inviscid consideration of the liquid. We refer to the mathematical model as the *potential flow model*, and the theoretical predictions arising from this mathematical model as the *potential flow theory*.

The potential flow theory predicts that, as the drop falls towards the solid surface, a buildup of air pressure underneath the drop causes the drop to deform in the middle, developing a *dimple*. The drop then spreads over a thin layer of gas that separates it from the substrate. The potential flow theory predicts scaling laws for the height of the gas layer. Subsequent experimental observations of the gas underneath the drop (Kolinski *et al.* 2012; van der Veen *et al.* 2012; de Ruiter

Symbol	Quantity	Order of magnitude	Units
P_0	Initial gas pressure	$\mathcal{O}(10^5)$	Pa
R	Initial drop radius	$\mathcal{O}(10^{-3})$	m
V_0	Initial drop velocity	$\mathcal{O}(10^{-1}$–$10^0)$	m/s
γ	Heat capacity ratio, gas	$\mathcal{O}(1)$	–
ρ_g	Density of gas	$\mathcal{O}(10^0)$	kg/m^3
ρ_l	Density of liquid	$\mathcal{O}(10^3)$	kg/m^3
ν_g	Kinematic viscosity of gas	$\mathcal{O}(10^{-5})$	m^2/s
ν_l	Kinematic viscosity of liquid	$\mathcal{O}(10^{-6}$–$10^{-4})$	m^2/s

Table 1: Relevant initial conditions and physical parameters, and their approximate values, which informs the mathematical model. The subscripts l and g denote the liquid drop and the gas, respectively, and 0 denotes initial conditions.

et al. 2012) show the existence of this dimple and the shape of the drop profile, similar to the predictions of the potential flow theory.

Experimental observations made by Kolinski *et al.* (2014*b*) in part of this parameter regime show that the falling drop first develops a dimple in the middle of the drop, as schematized by the liquid–gas interface shown in green in Figure 1(b). This is consistent with the potential flow theory (Mandre *et al.* 2009; Mani *et al.* 2010; Mandre & Brenner 2012). Subsequently in time, and prior to contact of the liquid–gas interface with the solid substrate, the shape of the interface depends on the kinematic viscosity of the liquid. Specifically, there is a critical time τ_c at which the minimum height of the drop from the substrate stops decreasing, and the *leading edge* of the drop begins to move away from the surface. The time τ_c is measured relative to the time when the drop would have made contact with the substrate if it were not deforming due to interactions with an intervening gas. Kolinski *et al.* (2014*b*) observe that $\tau_c \propto {\nu_l}^{1/2}$.

As a consequence of the discrepancy between the observations of Kolinski *et al.* (2014*b*), who definitively show the effect of liquid viscosity on the shape of the liquid–gas interface well before contact between the liquid and the substrate, and the potential flow theory, we are specifically interested in capturing the role of liquid viscosity, on these coupled dynamics. Based on the observations of Kolinski *et al.* (2014*b*), we modify the potential flow model to consider a liquid described by the full Navier–Stokes equations, rather than an inviscid approximation.

2.2. *Mathematical model*

The dynamics of an initially spherical drop are naturally described in terms of three-dimensional spherical polar co-ordinates, and those of the gas layer in terms of three-dimensional cylindrical polar co-ordinates. In this co-ordinate system, based on experimental observations of air layer profiles under an impacting drop (Kolinski *et al.* 2012; de Ruiter *et al.* 2012; van der Veen *et al.* 2012; Kolinski *et al.* 2014*b*,*a*, 2019), we first use the simplifying approximation of axisymmetric flow in the drop and the gas, with the axis of symmetry being perpendicular to the substrate, through the centre of the undeformed drop.

As in the potential flow model (Mandre *et al.* 2009; Mani *et al.* 2010; Mandre & Brenner 2012), we further simplify our consideration by approximating the

drop as initially being an infinite cylinder, with the long axis perpendicular to the substrate, rather than spherical. With these assumptions and approximations, we can describe the dynamics of the liquid and gas using two-dimensional Cartesian co-ordinates (x, y). The initial height $h(x, t = T_0)$ of the liquid–gas interface is described by a parabolic profile as

$$h(x, t = T_0) = H_0 + \frac{x^2}{2R}, \tag{2.1}$$

where H_0 is the initial height of the centre of the interface, i.e., at $x = 0$.

We model the flow in the liquid using the incompressible Navier–Stokes equations. The continuity equation for the liquid is

$$\nabla \cdot \mathbf{u}_l = 0, \tag{2.2}$$

and the momentum equation for the liquid is

$$\mathbf{u}_{l,t} + \mathbf{u}_l \cdot \nabla \mathbf{u}_l = -\frac{\nabla p_l}{\rho_l} + \nu_l \nabla^2 \mathbf{u}_l, \tag{2.3}$$

where $\mathbf{u}_l = (u_x, u_y)$, p_l and ρ_l are the velocity, pressure, and density of the liquid, respectively.

Based on the potential flow theory (Mandre *et al.* 2009; Mani *et al.* 2010; Mandre & Brenner 2012) and subsequent experimental observations (de Ruiter *et al.* 2012; van der Veen *et al.* 2012; Kolinski *et al.* 2014*b*), the gas layer is slender, with the horizontal length scale L_x being much greater than the vertical length scale L_y, allowing for an approximation of one-dimensional flow in the gas. The height $h = h(x, t)$ of the gas layer is thus described by the compressible lubrication equation (Taylor & Saffman 1957),

$$12\mu_g \left(\rho_g h\right)_t = \left(\rho_g h^3 p_{g,x}\right)_x, \tag{2.4}$$

and the equation of state is described by an adiabatic assumption,

$$\frac{p_g}{P_0} = \left(\frac{\rho_g}{\rho_0}\right)^{\gamma}. \tag{2.5}$$

The coupling of flows in the liquid and gas at their interface is done using the Laplace condition for pressure,

$$p_l = p_g + \sigma h_{xx}, \tag{2.6}$$

and equality of shear stress in the liquid and gas at the liquid–gas interface is

$$\tau_l(x, h) = \tau_g(x, h). \tag{2.7}$$

Far enough away from the deforming effects of the intervening gas layer on the liquid drop, the pressure in the gas is the ambient pressure, $\lim_{x\to\pm\infty} p_g(x, t) = P_0$.

Given that the initial and boundary conditions are symmetric about $x = 0$, we modify our mathematical model to incorporate symmetry boundary conditions about $x = 0$. We do so by applying the boundary conditions $(u, v_x) = (0, 0)$ in the liquid domain and $p_{g,x} = 0$ and $h_x = 0$ in the gas layer.

2.3. *Liquid domain and boundary conditions*

Having specified the physical problem in Section 2.1 and the mathematical model, with initial and boundary conditions, in Section 2.2, we now turn to a description

of the domain and boundary conditions that specify the flow in the liquid in a computationally tractable manner. The assumptions that lead to numerical approximations in this section are specified in Sections 2.1 and 2.2. We detail them here as appropriate.

2.3.1. *Rectangular domain with mass flux*

Following from the previous section, the liquid drop is described by a two-dimensional flow field. As the drop interacts with the gas layer, its shape changes. The drop begins to deform close to the middle of the interface, at $x = 0$. With this observation, we choose a region of interest, as shown in Figure 1(b), that stretches outwards from $x = 0$ and upwards from $y = h(x, t)$.

We make an additional approximation that the flow in the liquid at $y = h(x, t)$ can be approximated by the flow at $y = 0$. We can remove the spatial dependence because the liquid–gas interface is slender. We simulate the control volume with and without a temporal dependence $y = h(t)$, and do not observe a significant change in results. With these approximations, we are able to choose a rectangular, inertial control volume, stretching outwards from $x = 0$ and upwards from $y = 0$, whose size is chosen based on the relevant physical scales (Section 2.4). With the use of symmetry in the domain, as described in Section 2.2, we need to model only half of the control volume. We choose to model the right half, leading to the computational domain shown in Figure 1(c). In subsequent sections, we describe the boundary conditions at each of the boundaries in the computational domain.

2.3.2. *Treatment of the viscous term and bottom boundary condition*

Initially, the drop is moving at uniform vertical velocity, meaning that all spatial velocity gradients are zero, and $\nabla^2 \mathbf{u}_l = 0$. Deformation of the drop begins at $x = 0$. Our model consequently assumes that the shear stresses are small away from this region where the drop has deformed. In a two-dimensional flow, vorticity is introduced only through shear stresses at the boundary. The vorticity therefore spreads into the interior of the drop from the deformed interface. We thus model the drop as having a region close to $(x, y) = (0, 0)$, where viscosity is important, while far away from this region, $\nu_l \nabla^2 \mathbf{u}_l$ makes a negligible contribution to equation (2.3). A schematic of the region where viscosity is important in the deformed drop is shown by yellow in Figure 1(b) and (c). Consequently, we model the domain as having one boundary where viscous effects are important, which is the bottom boundary.

At the bottom boundary, we apply the boundary conditions specified in equations (2.6) and (2.7). Equation (2.7) is enforced through a condition on the gradient of the horizontal velocity,

$$u_{l,y}(x, 0) = \frac{\mu_g}{\mu_l} u_{g,y}(x, 0). \tag{2.8}$$

2.3.3. *Boundaries in the interior of the drop: top and right boundary conditions*

According to our approximation of a rectangular domain, the bottom boundary of the liquid interacts with the gas layer. The other boundaries are chosen to be in the interior of the drop, away from the effect of vorticity from the bottom boundary, and can be treated as inviscid. With this approximation, at these boundaries, denoted as *interior boundaries*, we simplify the momentum equation for the liquid, equation (2.3), by noting that the viscous term, $\nu_l \nabla^2 \mathbf{u}_l$, is relatively small.

Additionally, the velocity gradients in the liquid are initially zero. Away from the effects of the gas layer, the nonlinear advective term in the momentum equation, $\mathbf{u}_l \cdot \nabla \mathbf{u}_l$ in equation (2.3), will also be small. With these approximations, we obtain a simplified momentum equation for the liquid at these boundaries,

$$\mathbf{u}_{l,t} = -\frac{\nabla p_l}{\rho_l}. \tag{2.9}$$

We use this simplified momentum equation to obtain velocity boundary conditions at the interior boundaries. Taking the divergence of equation (2.9) and noting that the flow in the liquid is incompressible, we obtain $\nabla^2 p_l = 0$. Knowing the pressure at the bottom boundary, and approximating the liquid as a semi-infinite domain, we get an analytical expression for the pressure at the interior boundaries,

$$p_l(x, y) = \frac{1}{\pi} \int_{-\infty}^{\infty} p_l(s, 0) \frac{y}{(x - s)^2 + y^2} \, \mathrm{d}s. \tag{2.10}$$

Assuming that the domain is larger than the region where the pressure from the gas is non-zero, we numerically integrate over a finite length of the domain boundary to get the pressure at a particular (x, y) location along the interior boundaries. Given the pressure at the boundary, we integrate equation (2.9) in time to obtain velocity boundary conditions at the interior boundaries. The size of the region where vorticity is significant determines the size of the domain, and the locations of the interior boundaries, which are calibrated in simulation.

2.4. *Choice of domain*

We simulate the coupled dynamics of the liquid and gas over the time interval $0 \leqslant t \leqslant t^{\mathrm{end}}$, for a simulation domain of $0 \leqslant x \leqslant L$ and $0 \leqslant y \leqslant \beta L$, where β is the aspect ratio, for the liquid, and a domain of $0 \leqslant x \leqslant L$ for the gas. To set the size of the domain and duration of the simulation, we consider the initial dynamics as the drop falls toward the surface, and compare to the theoretical results of the potential flow theory (Mandre *et al.* 2009). We use the scaling results of the potential flow theory for the centre of the gas layer, $h(x = 0, t)$. The scaling analyses predict the height H^* at which the pressure buildup in the gas layer causes the drop to undergo significant deformation and develop a stagnation point at $x = 0$, forming a dimple.

According to potential flow theory, the compressibility of the flow in the gas is determined by the parameter

$$\epsilon \equiv \frac{P_0 RSt^{4/3}}{\mu_g V}, \tag{2.11}$$

which is the ratio of the initial gas pressure to the pressure that would have built up if the gas were treated as incompressible, where $St \equiv {}^{\mu_g}/_{\rho_l V R}$ (Mandre *et al.* 2009; Mani *et al.* 2010; Mandre & Brenner 2012; Langley *et al.* 2017).

The results of Kolinski *et al.* (2014*b*), showing the relationship between ν_l and the drop profile, correspond to $\epsilon^{-1} < 1$, meaning that the flow in the gas can be considered to be incompressible. While our simulations model the full incompressible flow in the gas, we use this approximation to set the initial conditions. In this regime, we have the estimate

$$H^* = RSt^{2/3}. \tag{2.12}$$

This scaling result is strictly valid for inviscid flow, $\nu_l = 0$, $Re \to \infty$, and no surface tension at the liquid–air interface, $\sigma = 0$, $We \to \infty$. While our simulations incorporate liquid viscosity and surface tension, equation (2.12) still provides a good estimate for the height at which the stagnation point forms, and is a useful measure of the physical scales of interest. We therefore set the initial height to be a multiple of H^*, so that

$$H_0 = \tilde{H}_0 H^* = \tilde{H}_0 RSt^{2/3}, \tag{2.13}$$

for a dimensionless constant $\tilde{H}_0$. Similarly, we set $t_{\text{end}} = \tilde{t}_{\text{end}} RSt^{2/3}/V$, and based on the parabolic shape of the initial profile we choose $L = \tilde{L} RSt^{1/3}$, where $\tilde{L}$ and $\tilde{t}_{\text{end}}$ are dimensionless constants.

3. Numerical implementation

In this section, we describe the numerical implementation of the mathematical model described in Section 2.2. Throughout the liquid domain, we compute and record the liquid velocity $\mathbf{u}_l$ and pressure p_l. In the gas layer, we compute and track the height h and pressure p_g. A reader may skip the remainder of this section without loss of continuity.

The flow-field variables ϕ are computed at discretized time steps, with simulation time $t = n\Delta t$, where Δt is the time step discretization used in the simulation, and n is an integer counter. Given values of field variables $\phi^{(n)} = \phi(t = n\Delta t)$, the goal of the simulation is to compute the field variables $\phi^{(n+1)}$. This section describes the numerical method for doing so, for the liquid flow-field variables, $\mathbf{u}_l$ and p_l, and gas flow-field variables, h and p_g.

3.1. *Projection method*

The core of the algorithm is based on Chorin's projection method (Chorin 1967, 1968), with further developments in the computational techniques behind the fluid simulation method (Bell *et al.* 1989; Almgren *et al.* 1998). In particular, the work of Almgren et al. (Almgren *et al.* 1996) introduces the approximate projection method discretized using the finite-element method (FEM). The numerical methods are described in detail by Sussman *et al.* (1999), Yu *et al.* (2003, 2007), and Rycroft *et al.* (2020). Here, we sketch the main features of these methods.

We solve for $\mathbf{u}_l$ and pressure p_l in the liquid domain by solving the momentum equation for the liquid, equation (2.3), subject to incompressibility of the liquid, as specified in equation (2.2). In describing the method for the solution of the field variables in the liquid domain, for the remainder of this section, we drop the subscript l.

The field variables are defined on a two-dimensional grid, discretized into rectangular cells of size Δx by Δy, as shown in Figure 2. The velocities $\mathbf{u}^n$ are located in the cell-centers, and the pressures p^n are located at the cell corners. To advance from step n to $n+1$, we first compute an intermediate velocity $\mathbf{u}^*$ according to

$$\frac{\mathbf{u}^* - \mathbf{u}^n}{\Delta t} = -\left[\mathbf{u} \cdot \nabla \mathbf{u}\right]^{n+1/2} + \frac{\nu}{2}\left(\nabla^2 \mathbf{u}^n + \nabla^2 \mathbf{u}^*\right). \tag{3.1}$$

Here, the viscous stress terms $\nu\nabla^2\mathbf{u}$ and $\nu\nabla^2\mathbf{u}^*$ are evaluated using a standard five-point finite-difference stencil. Due to the presence of the $\mathbf{u}^*$ on the right hand

side of equation (3.1), it must be solved implicitly. We use a multigrid method to solve the resulting linear system.

The advective term $[\mathbf{u} \cdot \nabla \mathbf{u}]^{n+1/2}$ is evaluated at the half-timestep $n + 1/2$ using the second-order Godunov upwinding scheme of Colella (1990). This is performed by extrapolating the velocity in each cell to midpoints of the four edges using a first-order Taylor expansion. Doing this requires that the gradient of the velocity is first evaluated at each cell center, which is done using the fourth-order monotonicity-limited scheme of Colella (1985). This scheme uses a five-point stencil in each coordinate, therefore requiring information from two grid points in each orthogonal direction.

After this procedure, each edge has two velocities from the two adjacent cells. A Godunov upwinding procedure is then used to select one based on the direction of the velocity. An intermediate marker-and-cell (MAC) projection is then used to adjust the velocities to satisfy a discrete zero divergence criterion, so that the net mass flow out of each cell is zero (Bell *et al.* 1991; Sussman *et al.* 1999). After this, the advective term can be accurately evaluated using centered finite differences of the upwinded edge-based velocities (Sussman *et al.* 1999; Yu *et al.* 2003, 2007; Rycroft *et al.* 2020).

The velocity at step $n + 1$ can be calculated from the intermediate velocity by evaluating the pressure gradient term,

$$\frac{\mathbf{u}^{n+1} - \mathbf{u}^*}{\Delta t} = -\frac{1}{\rho} \nabla p^{n+1}, \tag{3.2}$$

but this requires knowledge of the pressure field p^{n+1}, and there is no explicit update equation for this field in the incompressible limit. To proceed, we take divergence of equation (3.2) and enforce that $\nabla \cdot \mathbf{u}^{n+1} = 0$, according to equation (2.2). Hence,

$$\nabla \cdot \left[\Delta t \left\{ \frac{1}{\rho} \nabla p^{n+1} \right\} \right] = \nabla \cdot \mathbf{u}^*, \tag{3.3}$$

which is a Poisson equation for the pressure that can be solved. Once p^{n+1} is known, equation (3.2) can be used to evaluate $\mathbf{u}^{n+1}$ and complete the timestep from n to $n+1$. We solve equation (3.3) using the FEM discretization of Almgren et al. (Almgren *et al.* 1996). Here, each pressure value at a cell corner has a corresponding bilinear hat function over the four neighboring grid cells (Yu *et al.* 2003, 2007; Rycroft *et al.* 2020). Once the pressure is computed, the gradient in equation (3.2) is evaluated using centered finite differences of the pressure field values.

3.2. *Implementation of boundary conditions: ghost layers*

The boundary conditions are implemented by means of ghost layers. Around the boundaries of the two-dimensional liquid domain, there are two layers of additional grid points. Two layers are required in order to evaluate the fourth-order monotonicity-limited derivatives arising from the advective term. The boundary conditions are specified in these layers of grid points. These conditions are then used to compute the necessary gradients in equation (3.1).

The velocity boundary conditions at the top and right boundaries of the liquid domain, corresponding to the interior of the drop, and described in Section 2.3.3, are obtained through substituting the expression for pressure given by equation

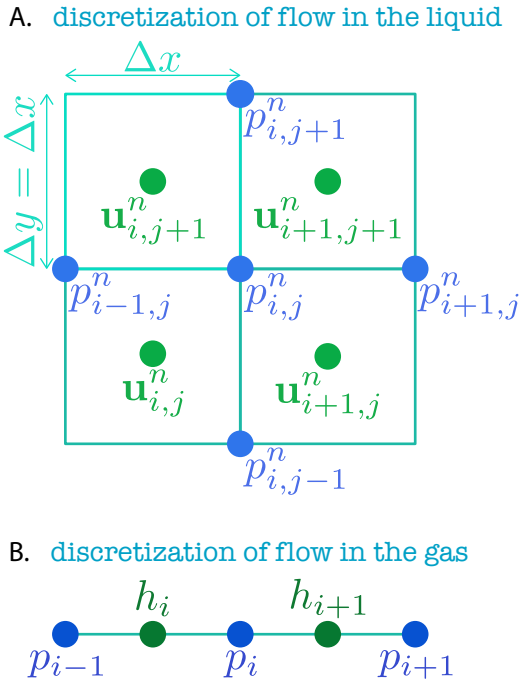

Figure 2: **Discretization of the field variables.** A: The two-dimensional computational grid for the liquid. B: The one-dimensional computational grid for the gas.

(2.10) in the expression for velocity at these boundaries, equation (2.9), and then using Simpson's rule to numerically integrate the pressure along these boundaries.

3.3. *Solution of the gas layer equations*

The field variables h and p_g for the gas layer are discretized in accordance with the discretization for the field variables for the liquid. Specifically, the pressure field p_g is stored at grid points in the same locations along the horizontal axis as the pressure field in the liquid, as shown in Figure 2. The height h is stored at grid points in the same locations along the horizontal axis as the velocity field $\mathbf{u}$ in the liquid.

As shown in Appendix A.1, substituting the equation of state (2.5) into the lubrication equation (2.4) yields

$$12\frac{\mu}{\gamma}hp_t + 12\mu h_t p = \frac{1}{\gamma}h^3 p_x p_x + 3h^2 h_x p p_x + h^3 p p_{xx}, \tag{3.4}$$

where the g subscript on the pressure has been dropped. We solve for this equation as follows:

(i) p is known at the time step $t^{(n)} = n\ \Delta t$
(ii) h, h_t, and therefore h_x are known at time step $t^{(n)} = n\ \Delta t$
(iii) solve for p at time step $t^{(n+1)} = (n+1)\ \Delta t$
(iv) use p as a boundary condition for the flow in the liquid, to obtain $v = h_t$ at time step $t^{(n+1)}$

To numerically solve equation (3.4) we discretize the spatial derivatives using second-order centered finite differences. To avoid a timestep restriction, we make use of the backward Euler method for discretizing the temporal derivative. Hence

we obtain the discretized form

$$12\frac{\mu}{\gamma}\bar{h}\left(\frac{p_i^{n+1}-p_i^n}{\Delta t}\right)+12\mu\bar{h}_t p_i^{n+1}=\frac{1}{\gamma}\bar{h}^3\left(\frac{p_{i+1}^{n+1}-p_{i-1}^{n+1}}{2\Delta x}\right)^2 + 3\bar{h}^2\bar{h}_x p_i^{n+1}\left(\frac{p_{i+1}^{n+1}-p_{i-1}^{n+1}}{2\Delta x}\right)+\bar{h}^3 p_i^{n+1}\left(\frac{p_{i+1}^{n+1}-2p_i^{n+1}+p_{i-1}^{n+1}}{\Delta x^2}\right), \quad (3.5)$$

that can be solved for the gas pressure p_i^{n+1}. In equation (3.5), the terms $\bar{h}$, $\bar{h}_t$, and $\bar{h}_x$ must be evaluated at the location of p_i^{n+1}. Since the height field is staggered with respect to the pressure field, this is done via linear interpolation and centered differencing, so that

$$\bar{h}=\frac{h_i+h_{i+1}}{2}, \qquad \bar{h}_t=\frac{h_{t,i}+h_{t,i+1}}{2}, \qquad \bar{h}_x=\frac{h_{i+1}-h_i}{\Delta x}. \quad (3.6)$$

Due to the products of pressure terms on the right hand side of equation (3.5), it is a nonlinear system of equations. We solve this using the Newton–Raphson method as described in Appendix A.2.

3.4. *Code implementation and parameter choices*

The simulations are performed using a custom code written in C++, using the OpenMP library for multithreading. The code makes use of the templated geometric multigrid (TGMG) library for solving the linear systems that arise when solving for the fluid. Each timestep requires four linear system solves: (1) to apply the MAC projection, (2) to apply the approximate FEM projection, and (3,4) to solve for the x and y velocity components when treating the viscous stress term implicitly. The code accepts a text configuration file as input, which sets all of the physical parameters, and describes the computational domain. The code and sample text configuration files are available on GitHub—see the data availability statement. The simulations are performed on a $M \times N$ grid for the liquid domain, and grid of length M for the gas layer. We choose the grid spacings to be equal, so that $\Delta x = \Delta y$. This implies that the aspect ratio β is equal to N/M.

Since the second derivative terms in both the liquid domain and the gas layer are handled implicitly, and the surface tension term in equation (2.6) is small, there is no timestep restriction in the simulation that scales like Δx^2 (Heath 2002). We therefore choose a candidate timestep to satisfy $\Delta t = \zeta \Delta x$ for a dimensionless constant ζ, based on satisfying Courant–Friedrichs–Lewy conditions (Courant *et al.* 1967) for the advective terms in the liquid domain and gas layer.

The simulation outputs N_f frames over the duration of the simulation. Thus the time between frames is $t_f = t_{\text{end}}/N_f$. In general, an integer multiple of candidate timesteps will not exactly match t_f, so that $c\Delta t < t_f < (c+1)\Delta t$. Because of this, the actual timestep is slightly adjusted to $\Delta t' = t_f/(c+1)$ and $c+1$ timesteps are taken between frames. Several examples demonstrating the performance of the code are provided in Appendix B.

4. Results and discussion

4.1. *Initial dynamics and comparison with potential flow theory*

To validate our approach, we first simulate the initial dynamics and we compare with the scaling results of potential flow theory that were introduced in Section 2.4

	Quantity	Value	Units
P_0	Initial gas pressure	10^5	Pa
R	Initial drop radius	1.5×10^{-3}	m
V	Initial drop velocity	0.45	m/s
γ	Heat capacity ratio, gas	1.4	–
σ	Interfacial surface tension	0.072	N/m
ρ_g	Density, gas	1.2754	kg/m^3
ρ_l	Density, liquid	997.96	kg/m^3
ν_g	Kinematic viscosity, gas	1.506×10^{-5}	m^2/s

Table 2: Baseline choices for the physical parameters used in the simulations. These parameters are used throughout the paper, with modifications to them noted in the text.

	Quantity	Initial dynamics, all values of ν_l	Lift-off, $\nu_l \leqslant 20\,\mathrm{mm}^2/\mathrm{s}$	Lift-off, $\nu_l > 20\,\mathrm{mm}^2/\mathrm{s}$
(M, N)	Grid dimensions	$(2048, 256)$	$(5120, 960)$	$(5120, 960)$
β	Aspect ratio	$1/8$	$16/3$	$16/3$
ζ	Timestep multiplier	8×10^{-3}	8×10^{-3}	8×10^{-3}
$\tilde{L}$	Domain width	30	30	45
$\tilde{H}_0$	Initial drop height	15	15	15
$\tilde{t}_{\mathrm{end}}$	Duration	50	50	100
N_f	Number of frames	250	250	250

Table 3: Baseline choices for the simulation parameters, which are all non-dimensional. The first set of parameters are for computing the initial dynamics and value of H^* in Section 4.1. The second two sets are for the lift-off calculations in all other sections. The procedure for connecting the non-dimensional variables $\tilde{L}$, $\tilde{H}_0$, and $\tilde{t}_{\mathrm{end}}$ to physical values is described in Section 2.4.

for the height of the stagnation point H^* (Mandre *et al.* 2009; Mani *et al.* 2010; Mandre & Brenner 2012). We use the baseline physical parameters given in Table 2. Since we only want to resolve the initial deceleration of the drop, and not the formation of the thin gas layer, we use the computational parameters in the third column of Table 3, which feature a relatively coarse numerical grid of size 2048×256. To compute H^*, we examine the sequence of height profiles from the simulation and find the time t^* when $h_t(0, t^*) = 0$, from which $H^* = h(0, t^*)$.

As described in Section 2.4, at low initial velocities the flow in the gas layer can be treated as incompressible, and the scaling result $H^* = RSt^{2/3}$ can be derived. Mani *et al.* (2010) extend this analysis to look at higher initial velocities, where compressibility of the gas becomes important. This happens at a height of

$$H_* = R(\mu_g V / R P_0)^{1/2}, \tag{4.1}$$

where the subscript '$*$' is used to distinguish from the stagnation height. By modeling the subsequent drop deceleration below H_* assuming gas compressibility, Mani *et al.* (2010) derive the result

$$H^*_{\mathrm{comp}} = RSt^{2/3} \epsilon^{(2-\gamma)/(2\gamma-1)} \tag{4.2}$$

for the stagnation height.

We first performed sequences of simulations using low initial velocites over the range from $V = 0.15\,\mathrm{m/s}$ to $V = 1.35\,\mathrm{m/s}$, using four different liquid viscosities from $\nu_l = 10\,\mathrm{mm^2/s}$ to $\nu_l = 300\,\mathrm{mm^2/s}$. We also ran two sets of simulations with the surface tension set to half and zero its baseline value. Figure 3(a) shows a plot of $H^*/(RSt^{2/3})$ as a function of ϵ^{-1}, with these six sets of data points in the left half of the domain where $\epsilon^{-1} < 1$ and gas compressibility is not important. We see that $H^*/(RSt^{2/3})$ is approximately constant and is in agreement with equation (2.12). To examine the trends more clearly, Figure 3(b) shows a zoomed-in plot of the same data. As expected, the best agreement is achieved for the smallest value of ν_l and for zero surface tension. For $\epsilon^{-1} < 1$, the values of $H^*/(RSt^{2/3})$ are slightly lower for the cases of larger ν_l and σ. The decrease in height of the stagnation point as ν_l increases is qualitatively consistent with the experimental observations of Langley *et al.* (2017), and hints at the limits of the potential flow theory (Mandre *et al.* 2009; Mani *et al.* 2010). By performing experiments with viscosities of up to $2 \times 10^6\,\mathrm{mm^2/s}$, Langley *et al.* (2017) are able to demonstrate that the centerline air thickness (closely related in definition to H^*) scales like $\mu_l^{-1/9}$. However, since we use inviscid boundary conditions on the top and sides of the fluid domain, we are unable to simulate large viscosities to compare to this result. Modifying our boundary conditions to work with large viscosities remains a subject for future work.

We also performed two sequences of simulations with higher initial velocities from $V = 1\,\mathrm{m/s}$ to $V = 18\,\mathrm{m/s}$ using $\nu_l = 10\,\mathrm{mm^2/s}$, to examine the compressible regime. However, we note from equation (2.13) that our usual choice for initial height scales according to $V^{-2/3}$, whereas from equation (4.1), the height where compressibility is important scales according to $V^{1/2}$. To fully capture the compressible effects, the drop must start higher than H_*, and thus the usual initialization procedure is problematic for large V. For these simulations we therefore set H_0 at a fixed value based on using $V = 2\,\mathrm{m/s}$ in equation (2.13). We ran two sequences of simulations using the usual choice of $\gamma = 1.4$, and another with $\gamma = 1$; as shown in Figure 3, these results are in very good agreement with the scalings of $\epsilon^{1/3}$ and ϵ, respectively, that are expected from equation (4.2).

4.2. *Evolution of dynamics and effect of liquid viscosity*

With the initial dynamics validated, we now turn attention to simulating the continued spreading of the liquid drop on a layer of gas, and the effect of viscosity on the evolution of the liquid–gas interface. We use the same baseline physical parameters given in Table 2, but since we must now accurately resolve the gas layer as it becomes very thin, we increase the simulation resolution as shown in the fourth and fifth columns of Table 3. Furthermore, since the deviation of the interface from the solid surface happens later for high viscosities (Kolinski *et al.* 2014*b*), we use a larger domain and longer duration when $\nu_l > 20\,\mathrm{mm^2/s}$, as indicated in the fifth column of Table 3. We begin by using the baseline initial drop velocity of $V = 0.45\,\mathrm{m/s}$ to match the experiments of Kolinski *et al.* (2014*b*).

Figure 4 shows the height profiles for three different simulations using liquid viscosities of $\nu_l = 10\,\mathrm{mm^2/s}$, $\nu_l = 32\,\mathrm{mm^2/s}$, and $\nu_l = 100\,\mathrm{mm^2/s}$. Panels (a), (b), and (c) show a large-scale view, where the initial parabolic profile approaches the surface, begins to decelerate and deforms to create the dimple. After the drop continues to fall, a thin layer of gas from $x \gtrapprox 200\,\mu\mathrm{m}$ is created and spreads

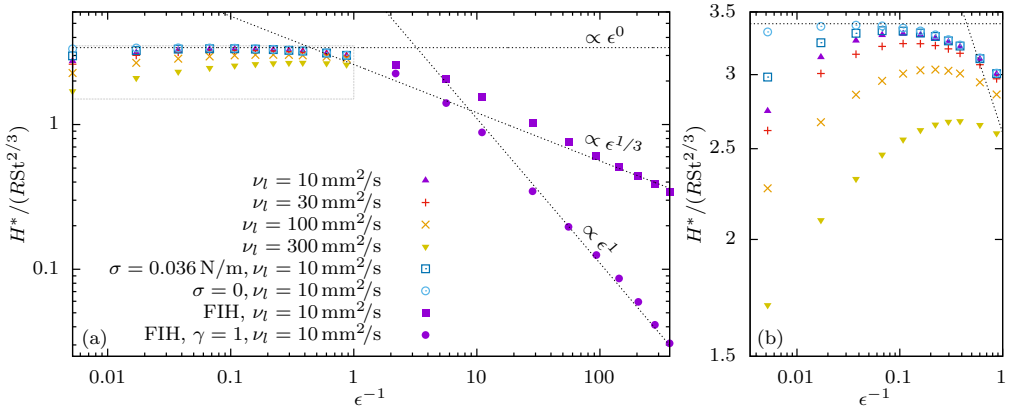

Figure 3: (a) Plot of rescaled initial stagnation height $H^*/(R\mathrm{St}^{2/3})$ as a function of the inverse of the dimensionless compressibility parameter $\epsilon = P_0 R\mathrm{St}^{4/3}/\mu_g V$, for a range of different liquid viscosities ν_l, surface tensions σ, and gas parameters γ. Unless otherwise stated, baseline parameters from Table 2 and Table 3 are used. By default, the drop starts from a height H_0 scaled according to equation (2.13). For $\nu_l = 10\,\mathrm{mm}^2/\mathrm{s}$, to account for compressibility effects, data from two simulation sequences that use a fixed initial height (FIH) based on substituting $V = 2\,\mathrm{m/s}$ into equation (2.13) are shown. (b) Zoomed-in plot of the same data, showing the region bounded by the dotted gray rectangle in panel (a).

outward. In all three simulations, the height profiles have a front that sweeps outward as more liquid approaches the surface.

Figure 5 shows snapshots of the pressure and vorticity in the liquid domain for the simulation with with $\nu_l = 10\,\mathrm{mm}^2/\mathrm{s}$. At $t = 24.02\,\mu\mathrm{s}$, the drop is still approaching the surface. The pressure builds up close to $x = 0$. Since the liquid near $x = 0$ is decelerated faster, this creates a region of negative vorticity over $0 \lessapprox x \lessapprox 250\,\mu\mathrm{m}$. By $t = 72.05\,\mu\mathrm{s}$, the thin layer of gas has formed, and the position of the front from Figure 4(a) is marked with a small triangle. There is a region of large positive pressure behind the front, a small region of negative pressure ahead of it. The contour of zero vorticity follows the front as it moves outward to $t = 96.07\,\mu\mathrm{s}$. The pressure fields are similar to those reported by Philippi *et al.* (2016), who also compute the pressure in the interior of the drop, using a different simulation framework (Popinet 2003, 2009; Lagrée *et al.* 2011).

Figure 4(d–f) shows zoomed-in plots of the height profiles in the thin layer for the three simulations. Behind the front, the height profiles align on top of each other, and trace out relatively stable envelopes, appearing as thick blue lines in Figure 4(d–f). In all three cases the envelopes initially slope downward before curving upward, indicating the deviation of the liquid–gas interface away from the solid surface, prior to contact between the solid and the liquid. This is the lift-off phenomenon (Kolinski *et al.* 2014*b*). Lift-off occurs more quickly for lower viscosities, and the envelope slopes upward faster. These results are in close agreement with the experimental results of Kolinski *et al.* (2014*b*).

We now quantify the lift-off time and position. While the envelopes in Figure 4(d–f) are relatively well defined, the height profiles shift slightly in over time, making it difficult to precisely define the moment of lift-off. However, close inspection of Figure 4(d–f) shows that in all cases, the height profiles have a leading tip that dips slightly below the envelope that forms. We found this to be a well-defined

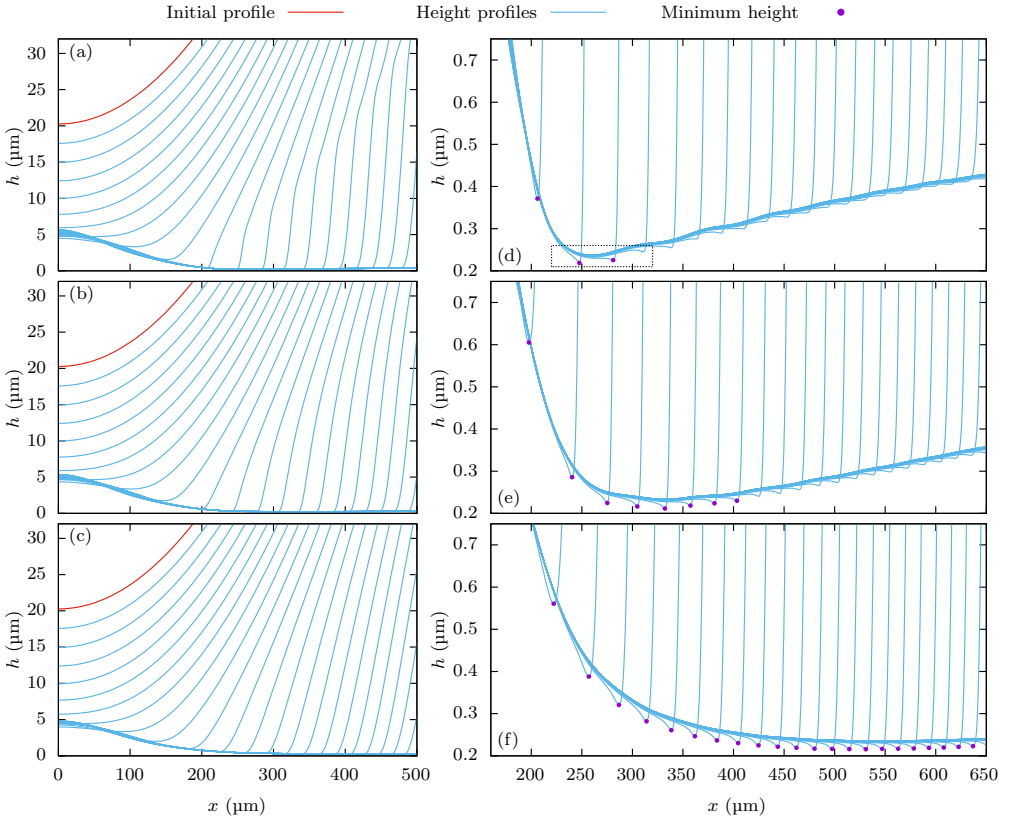

Figure 4: Profiles of the height $h(x,t)$ of the gas layer at intervals spaced 6.004 µs apart, corresponding to an integer multiple of the frame output interval t_f described in Section 3.4, for liquid viscosities of (a) $\nu_l = 10\,\mathrm{mm}^2/\mathrm{s}$, (b) $\nu_l = 32\,\mathrm{mm}^2/\mathrm{s}$, and (c) $\nu_l = 100\,\mathrm{mm}^2/\mathrm{s}$. All other simulation parameters follow the baseline values in Table 2 and Table 3. Panels (d), (e), and (f) show the same data as (a), (b), and (c), respectively, but with a smaller range of h to highlight the lift-off behavior. For each profile, the global minimum, which follows the leading tip, is also plotted on the curves; once the global minimum is no longer at the leading tip, it is no longer plotted. The dashed box in panel (d) marks a further zoomed-in region shown in Figure 6.

feature that occurs universally across all of our simulations. The tip position can be determined as the global minimum of the height profile at each time, and provides a way to precisely define when lift-off occurs, at the moment when the leading tip starts to rise.

Figure 6(a) shows a further zoomed-in plot of the height profiles during lift-off for the case of $\nu_l = 10\,\mathrm{mm}^2/\mathrm{s}$. Once the leading tip has risen sufficiently, then it is no longer the global minimum. However, since lift-off has always occurred by the time the leading tip is rising, this does not cause any difficulty in identifying the lift-off time. It is natural to consider whether the leading tip is a real feature or a numerical artifact that emerges from discretization error and limited resolution. To address this, Figure 6(b) shows a further zoomed-in region, depicting the leading tip in detail. Here, the blue circles show individual simulation grid points. The grid spacing is substantially smaller than the width of the leading tip, indicating that it is a real feature. Further numerical tests of accuracy are provided in Appendix C.

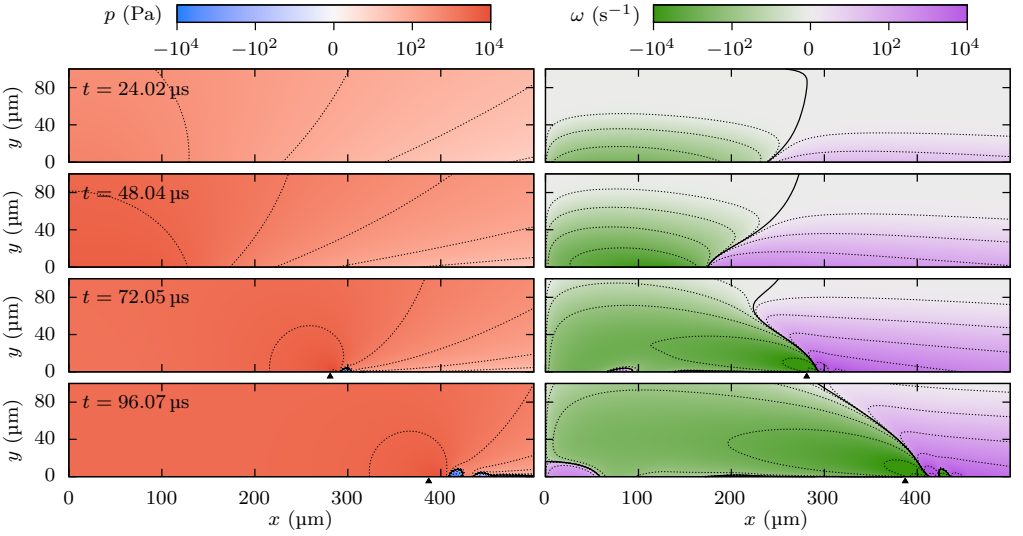

Figure 5: Snapshots of pressure, p, (left) and vorticity, $\omega = [\nabla \times \mathbf{u}]_3$, for a portion of the liquid domain for a simulation with liquid viscosity $\nu_l = 10\,\mathrm{mm}^2/\mathrm{s}$, where all other parameters follow the baseline values in Table 2 and Table 3. The field values exhibit large variations in scale and also switch sign, so a nonlinear mapping $f(\alpha) = \frac{1}{\log 10} \sinh^{-1} \frac{\alpha}{2}$ is used to create the color maps. The thick black lines indicate the zero contour. The thin black lines show contours for $\pm 10^{n/2}$ Pa for pressure and $\pm 10^n\,\mathrm{s}^{-1}$ for vorticity, where $n \in \mathbb{N}_0$. For $t = 72.05\,\mu\mathrm{s}$ and $t = 96.07\,\mu\mathrm{s}$ the position of the front (given by the local minimum of the profiles in Figure 4(a,d)) is marked with a triangle.

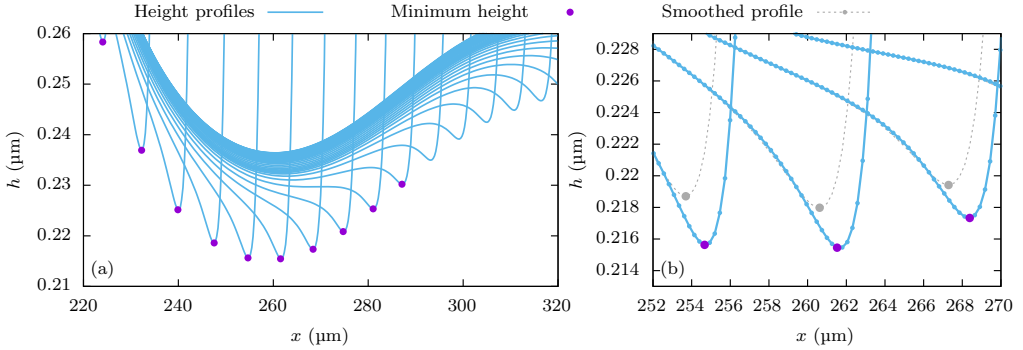

Figure 6: Zoomed-in plots of the height of the gas layer at intervals spaced 1.2009 µs apart for liquid viscosity $\nu_l = 10\,\mathrm{mm}^2/\mathrm{s}$, where all other parameters follow the baseline values in Table 2 and Table 3. Panel (a) shows the region marked by the dashed box in Figure 4(d). For each profile, the global minimum, which follows the leading tip, is also plotted on the curves; once the global minimum is no longer at the leading tip, it is no longer plotted. Panel (b) shows the region marked by the dashed box in panel (a). In panel (b), the small blue circles indicate the computational grid. The gray dashed lines show the profiles with Gaussian smoothing applied, and the gray circles show the global minima of the smoothed lines.

The width of the tip is governed by surface tension. While many of our simulations use the baseline value of $\sigma = 0.072\,\mathrm{N/m}$ from Table 2, we also consider reduced surface tension where the tip becomes sharper. In this case, there can be numerical difficulties in identifying the minimum due to per-gridpoint

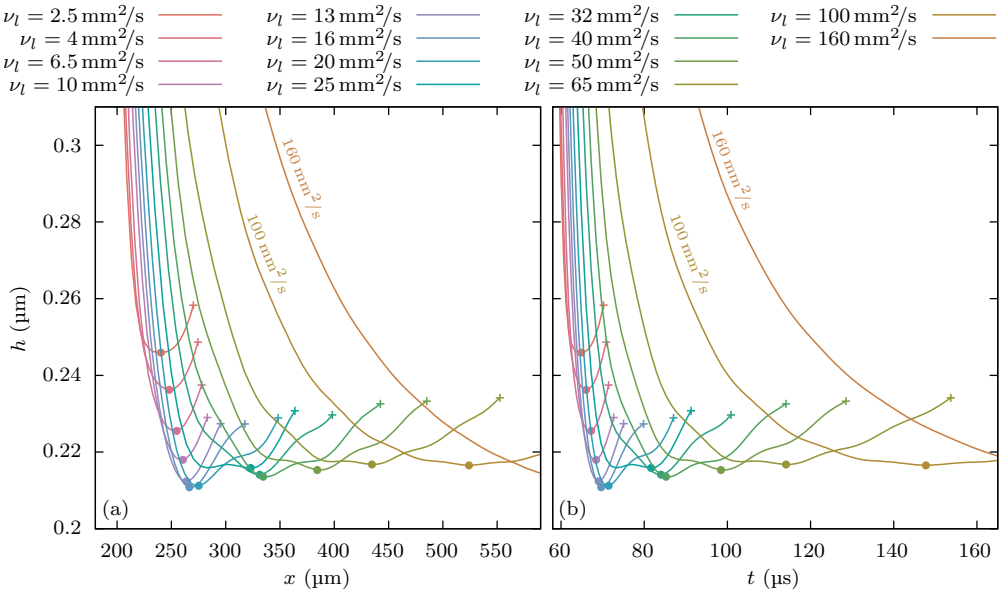

Figure 7: Trajectories of the global minimum of the drop profile in (a) the (x, h) plane, and (b) the (t, h) plane for the baseline parameters with initial drop velocity $V = 0.45\,\mathrm{m/s}$, for a range of different liquid viscosities. All other parameters follow the baseline values in Table 2 and Table 3. For each trajectory, the filled circle indicates where the global minimum reaches its lowest point, which we define as when lift-off occurs. Each cross indicates when the global minimum no longer marks the leading tip. Trajectories for selected ν_l are labeled.

variations in the height profile. To create a scheme for identifying the minimum across all simulations, we therefore smooth the height profile using a Gaussian kernel with length scale 1.2 µm. This results in a minimal alteration in the leading tip position (Figure 6(b)), but improves robustness when analyzing the simulations. Numerically, the global minimum is found by identifying the local minima of the cubic interpolant of the smoothed profile, and selecting the smallest one.

Figures 7 and 8 show trajectories of the leading tip for a range of viscosities, from $\nu_l = 2.5\,\mathrm{mm^2/s}$ to $\nu_l = 160\,\mathrm{mm^2/s}$, for drop impact velocities of $V = 0.45\,\mathrm{m/s}$ and $V = 0.9\,\mathrm{m/s}$, respectively. The distance x that characterises the horizontal extent of the dimple, as shown in Figures 7(a) and 8(a), is closely matches the experimental results of Kolinski *et al.* (2014*b*) and Langley *et al.* (2017), respectively. The height of the gas layer, $h \sim \mathcal{O}(100)\,\mathrm{nm}$, is also in a similar regime as the experimental observations of Kolinski *et al.* (2014*b*) and Langley *et al.* (2017), though larger in value than the h observed by Kolinski *et al.* (2014*b*).

In Figure 7, two regimes are visible. For $\nu_l \lessapprox 20\,\mathrm{mm^2/s}$, increasing viscosity results in the trajectory reaching a lower value of h, and the lift-off position moving slightly outward. For $\nu_l \gtrapprox 20\,\mathrm{mm^2/s}$, increasing viscosity results in the trajectory reaching a higher value of h, and the lift-off position moves outward substantially. Small undulations in the trajectories are visible for $\nu_l \gtrapprox 20\,\mathrm{mm^2/s}$, which arise due to capillary waves in the height profile. This can have a substantial effect on the measured lift-off time, depending on which undulation achieves the global minimum. For example, there is a large difference between $\nu_l = 20\,\mathrm{mm^2/s}$ and $\nu_l = 25\,\mathrm{mm^2/s}$. In Figure 8, for $V = 0.9\,\mathrm{m/s}$, the scale of h is smaller. The observed reduction in film thickness with increasing V is consistent with the experimental

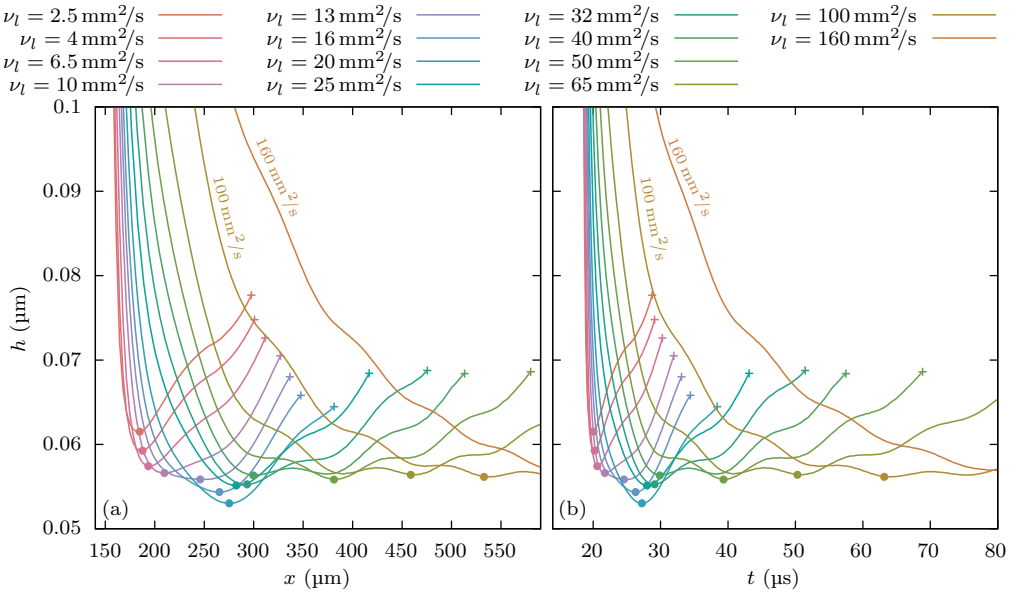

Figure 8: Trajectories of the global minimum of the drop profile in (a) the (x, h) plane, and (b) the (t, h) plane for the baseline parameters with initial drop velocity $V = 0.9\,\mathrm{m/s}$, for a range of different liquid viscosities. All other parameters follow the baseline values in Table 2 and Table 3. For each trajectory, the filled circle indicates where the global minimum reaches its lowest point, which we define as when lift-off occurs. Each cross indicates when the global minimum no longer marks the leading tip. Trajectories for selected ν_l are labeled.

observations of Kolinski *et al.* (2014*b*). Considering the case of liquid–substrate contact being mediated by a reduced thickness of the air layer, our observations are also consistent with the transition from gliding over an air layer to contact with increasing V, as reported by Langley *et al.* (2017). Figure 8 also shows a larger relative amplitude of the capillary waves as compared to the smaller impact velocity of Figure 7. As a result, the capillary waves have a noticeable effect on lift-off times at lower viscosities, with a large difference in lift-off time between $\nu_l = 10\,\mathrm{mm^2/s}$ and $\nu_l = 13\,\mathrm{mm^2/s}$.

We now compare to the experimental finding of Kolinski *et al.* (2014*b*) that the lift-off time is proportional to $\nu_l^{1/2}$. The lift-off time τ in this previous work is defined relative to a time origin of when the drop would reach $h = 0$ in the absence of the surface. Here, since the initial height h_0 and velocity V are known, we compute the time origin as $t_0 = h_0/V$. By contrast, Kolinski *et al.* (2014*b*) were not able to directly view h_0, since the drop can only be observed once it enters an evanescent field of height $h_{\mathrm{ev}} = 1\,\mu\mathrm{m}$. Instead, they measured the first position and time (h', r', t') when the drop enters the evanescent field, and assume that the drop is undeformed at this position, so that $h' = h_0 - Vt' + r'^2/(2R^2)$. Hence h_0 can be calculated, and therefore the time origin is $t_0^{\mathrm{exp}} = h_0/V - t' + r'^2/(2R^2V)$.

Figure 9 shows the lift-off times τ as a function of viscosity for seven different values of initial velocity V. The data points from Kolinski *et al.* (2014*b*) are also plotted. Even though the experiments of Kolinski et al. are performed in a three-dimensional axisymmetric configuration, there is good quantitative agreement with the two-dimensional simulation results.

Overall, the results are consistent with the $\nu_l^{1/2}$ scaling result, but the additional

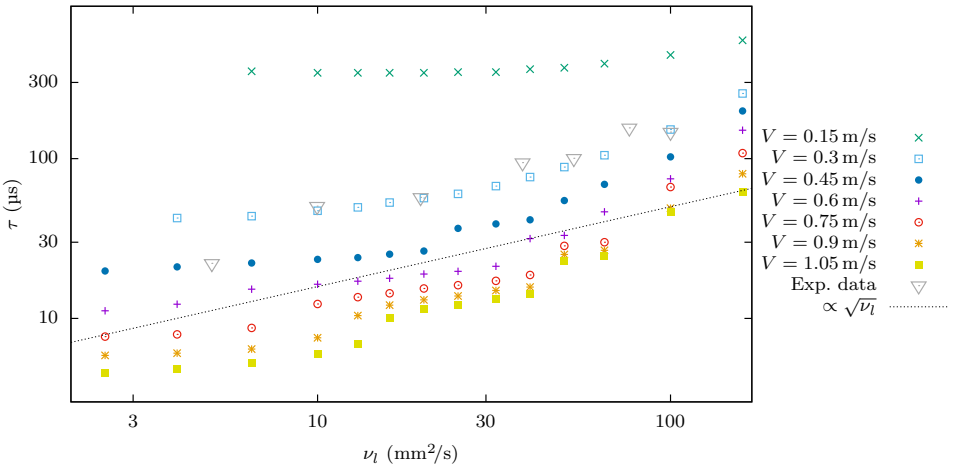

Figure 9: Liftoff time τ as a function of liquid viscosity ν_l, for a range of initial drop velocities V. All other parameters follow the baseline values in Table 2 and Table 3. The experimental data is taken from Figure 4(a) of the paper by Kolinski *et al.* (2014*b*), which used $V = 0.45$ m/s. Three data points are omitted from the plot for low V and low ν_l due to physical difficulties with running the simulation—see Section 4.3.

precision provided by the simulations reveals a more complicated relationship between ν_l and τ. For each value of V, the data points exhibit some fluctuations, which are due to the undulations visible in Figure 7 where the global minimum defining the lift-off time may abruptly change. While a $\nu_l^{1/2}$ scaling appears consistent with the high impact velocities where $V \gtrapprox 0.75\,\mathrm{m/s}$, the data for low impact velocities looks better fit to ν_l^{η}, where there are two different values of η with a change at $\nu_l \approx 20\,\mathrm{mm^2/s}$. This is also consistent with the two different types of behavior observed in Figure 7.

The slope of data points for small values of ν_l in Figure 9 is strongly affected by the choice of time origin, and may affect the conclusions about the relevant exponents. To investigate this further, we replotted the data using t_0^{exp} as the time origin; this resulted in small shift upwards of the data (since $t_0^{\mathrm{exp}} < t_0$ in all cases), but did not affect the overall patterns. As a third approach, we defined a time origin t_0^{dat} directly from the data, by finding the best fit to the model $\tau_{\mathrm{dat}} = t - t_0^{\mathrm{dat}} = \gamma(\nu_l/\nu_{\mathrm{sc}})^{\alpha}$ for the three free parameters $(t_0^{\mathrm{dat}}, \gamma, \alpha)$. Here $\nu_{\mathrm{sc}} = 20\,\mathrm{mm^2/s}$ is chosen as an arbitrary viscosity scale. Specifically, for the data points $(\nu_{l,k}, t_k)$, we minimized the residual

$$S(t_0^{\mathrm{dat}}, \gamma, \alpha) = \frac{1}{2}\sum_k \left(\log\gamma + \alpha \log\frac{\nu_{l,k}}{\nu_{\mathrm{sc}}} - \log(t_k - t_0^{\mathrm{dat}})\right)^2. \tag{4.3}$$

We used the L-BFGS-B algorithm for bound-constrained nonlinear optimization (Byrd *et al.* 1995), and enforced $t_0^{\mathrm{dat}} < 0.999 t_{\mathrm{min}}$ and $\alpha > 0$, where $t_{\mathrm{min}} = \min_k\{t_k\}$. We started the minimization using multiple initial guesses with $t_0^{\mathrm{dat}} \in [0.7t_{\mathrm{min}}, 0.9t_{\mathrm{min}}]$ and $\alpha \in [0.4, 1.2]$. For each pair $(t_0^{\mathrm{dat}}, \alpha)$ the value of γ is set so that the bracketed expression in equation (4.3) is zero for the $\nu_l = 20\,\mathrm{mm^2/s}$ data point, so that the initial guess should be close to the minimum of S.

Figure 10 shows a replotting of the data relative to this time origin. The data for

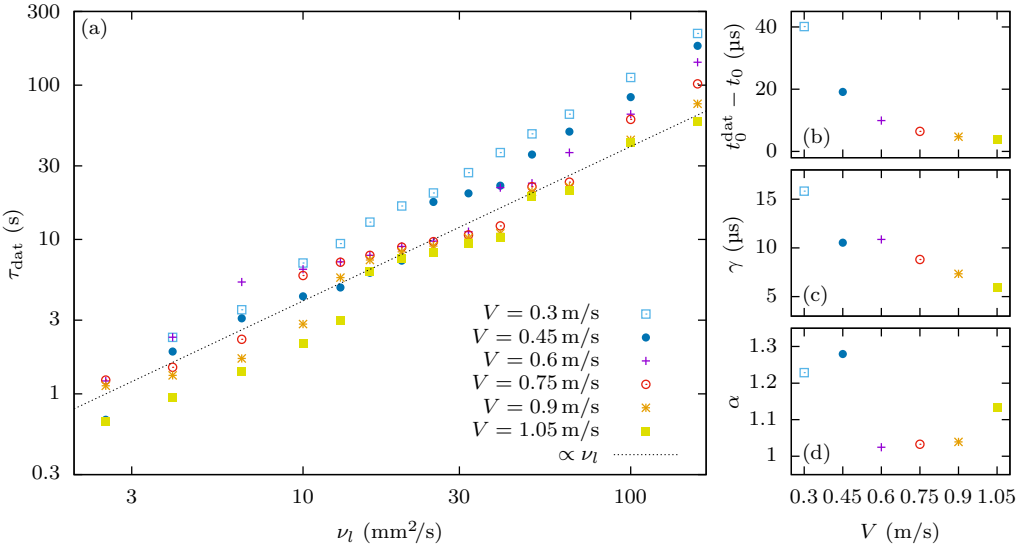

Figure 10: (a) Liftoff time τ_{dat} as a function of liquid viscosity ν_l, for a range of initial drop velocities V, using the alternative time origin definition based on minimizing the three-parameter residual function in equation (4.3). All other parameters follow the baseline values in Table 2 and Table 3. (b–d) best fits of the parameters $t_0^{\mathrm{dat}} - t_0$, γ, and α for different initial drop velocities.

$V = 0.15$ m/s is omitted from this plot since the lift-off times are non-monotonic for the smallest values of ν_l. For each other value of V, the minimization procedure converges to a single unique solution for all initial guesses. With this definition of time origin, all of the data is more consistent with a linear scaling relationship as opposed to the square root relationship in Figure 9. Panels (b), (c), and (d) show the values of the fitted parameters, and demonstrate that $\alpha \in [1.02, 1.28]$ in all cases. The average residual over the six different values of V is $\bar{S} = 0.2536$. If the exponent is constrained to $\alpha = \frac{1}{2}$ to match the exponent of Kolinski *et al.* (2014*b*) then the average residual increases to $\bar{S} = 0.3855$ and the data points exhibit an upward curve in a log–log plot that systematically deviates from a power law. Constraining the exponent to $\alpha = 1$ results in $\bar{S} = 0.2805$ and a better fit to the model that is similar to the three-parameter fit shown in Figure 10. See the Supplementary Information for additional discussion and parameter fits. These results highlight that any theoretical analysis of the relationship between τ and ν_l would need to take into account the sensitivity of defining the time origin.

Figure 11(a) shows lift-off times (relative to t_0) for for three different drop radii: the original value of $R = 1.5$ mm, and as well as half and double this value. Increasing the radius increases the lift-off time, similar to the effect of lowering velocity in Figure 9.

4.3. *The role of surface tension*

The simulations allow us to change the surface tension in ways that would be difficult to do experimentally, to investigate the importance of this physical effect. Changing the surface tension allows us to suppress or accentuate the capillary waves in the liquid–gas interface, as shown in Figure 7, to investigate the effect of surface tension on the phenomenon of lift-off. Following the same procedure as in Section 4.2, we calculated the lift-off times for $\sigma = 0.0072$ N/m, $\sigma = 0.036$ N/m

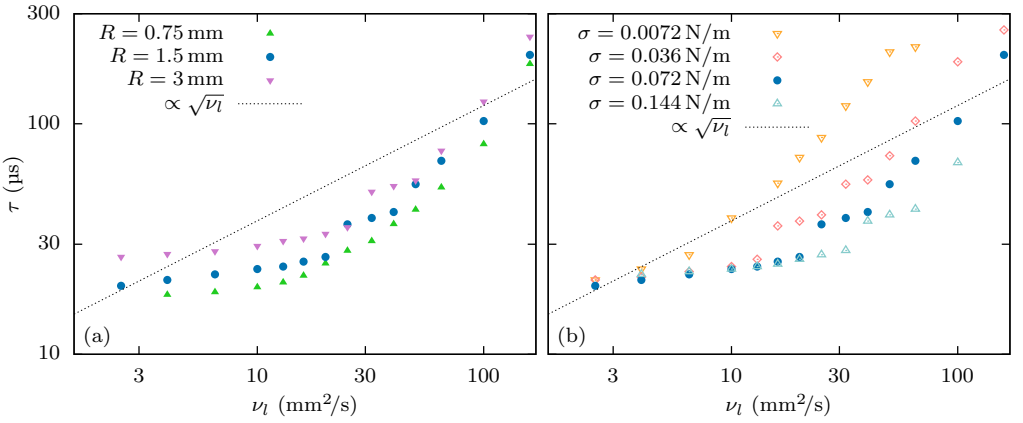

Figure 11: Lift-off time as a function of liquid viscosity, for a range of (a) different drop radii, and (b) different surface tension values. All other parameters follow the baseline values in Table 2 and Table 3. The data point for $(\nu_l, R) = (2.5\,\mathrm{mm}^2/\mathrm{s}, 0.75\,\mathrm{mm})$ is omitted due to physical difficulties with running the simulation (Section 4.3). The data points for $\sigma = 0.0072\,\mathrm{N/m}$ and $\nu_l \geqslant 100\,\mathrm{mm}^2/\mathrm{s}$ are omitted because lift-off does not occur over the simulation duration.

and the $\sigma = 0.144\,\mathrm{N/m}$, corresponding to a tenth, half, and double the usual surface tension values, respectively. Figure 11(b) shows that as surface tension is reduced, the lift-off times increase markedly. For the case of $\sigma = 0.0072\,\mathrm{N/m}$ lift-off is eliminated for large values of ν_l, with the leading tip continuing to decrease over the course of the simulation.

Figure 11(b) strongly suggests that surface tension is important in creating lift-off. Reducing from $\sigma = 0.036\,\mathrm{N/m}$ to $\sigma = 0.0072\,\mathrm{N/m}$ almost doubles the lift-off times in most cases, and one can ask whether lift-off will be completely eliminated in the limit as surface tension vanishes. To examine this, we ran a sequence of simulations with $\sigma = 0$, with several representative examples for $\nu_l = 10\,\mathrm{mm}^2/\mathrm{s}$, $\nu_l = 32\,\mathrm{mm}^2/\mathrm{s}$, and $\nu_l = 100\,\mathrm{mm}^2/\mathrm{s}$ shown in Figure 12. This is a difficult limit to probe in our simulations, since as discussed for Figure 6, surface tension regularizes the leading tip. Figure 13 shows close-ups of the profiles for $\nu_l = 10\,\mathrm{mm}^2/\mathrm{s}$, indicating that the leading tip becomes as sharp as a single grid point, and the minima of the profiles can fluctuate non-monotonically depending on exactly how the tip aligns with the computational grid. However, in this case the profile smoothing procedure introduced in Section 4.2 is sufficient to extract smooth leading tip trajectories.

The very sharp leading tip causes another difficulty in the simulations: as the tip is advected across the computational grid, there will be an effective numerical diffusion, which will act as though a small surface tension has been imposed. This is an important issue since Figure 11(b) already confirms that small surface tensions can considerably alter the behavior. To test this, we compared simulations with the baseline parameters to those on a finer grids (Appendix C). Unlike the case for finite surface tension, the simulations on a finer grids are noticeably different, with the profiles reaching lower heights and the leading tip not curving up as rapidly. Since liquid viscosity also regularizes the evolution of the height profile, these discrepancies are more significant when ν_l is small.

We calculated the trajectories of the leading tip for a range of values for liquid viscosity, ν_l. For $13\,\mathrm{mm}^2/\mathrm{s} < \nu_l \leqslant 40\,\mathrm{mm}^2/\mathrm{s}$ we switched to a larger computational

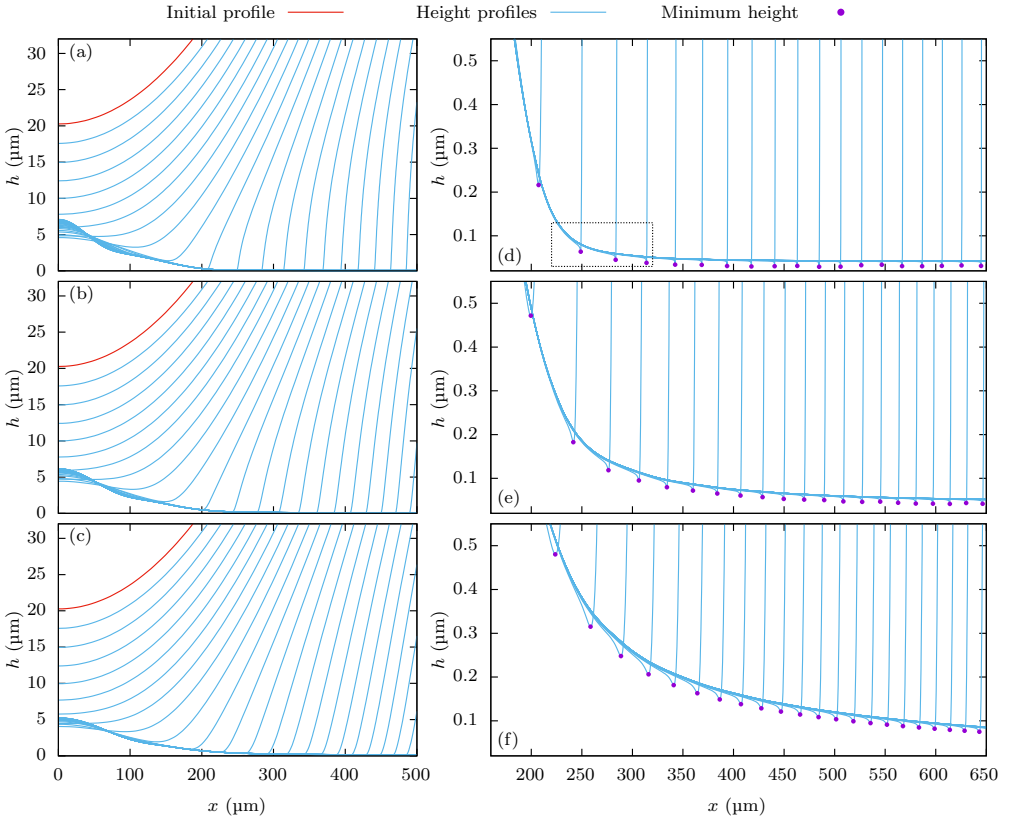

Figure 12: Profiles of the height of the gas layer at intervals spaced 6.004 µs apart for liquid viscosities of (a) $\nu_l = 10\,\mathrm{mm}^2/\mathrm{s}$, (b) $\nu_l = 32\,\mathrm{mm}^2/\mathrm{s}$, and (c) $\nu_l = 100\,\mathrm{mm}^2/\mathrm{s}$ using zero surface tension. All other parameters follow the baseline values in Table 2 and Table 3. Panels (d), (e), and (f) show the same data as (a), (b), and (c), respectively, but with a smaller range of h to highlight that no lift-off occurs in this case. For each profile, the global minimum, which follows the leading tip, is also plotted on the curves. The dashed box in panel (d) marks a further zoomed-in region shown in Figure 13.

grid of size 8192×1536, and for $\nu_l \leqslant 13\,\mathrm{mm}^2/\mathrm{s}$ we switched to a very large grid of size 12288×2304. For $\nu_l \leqslant 44\,\mathrm{mm}^2/\mathrm{s}$ we were not able to simulate on a large enough grid to adequately resolve the numerical diffusion, and hence results in this range are omitted. Figure 14 shows the trajectories in both the (x, h) and (t, h) planes. In all cases, the leading tips continue to decrease. While our results only examine one particular set of physical parameters (from Table 2) our results strongly suggest that surface tension is required for lift-off to occur. Moreover, we observe that the thickness of the gas layer increases with ν_l. This is consistent with the experimental findings of Langley *et al.* (2017), who observe a transition from drop–substrate contact to gliding of the drop over a thin air film as ν_l increases.

We also found a regime where the effect of surface tension can qualitatively affect the lift-off behavior. Figure 15(a) shows the height profiles for a simulation with the baseline value of surface tension of $\sigma = 0.072\,\mathrm{N/m}$ in the regime of low initial velocity, $V = 0.3\,\mathrm{m/s}$ and low viscosity, $\nu_l = 6.5\,\mathrm{mm}^2/\mathrm{s}$. In this regime, prominent capillary waves are generated outside the thin gas layer, which grow larger as time progresses. Figure 15(b) shows a zoomed-in plot of the profiles

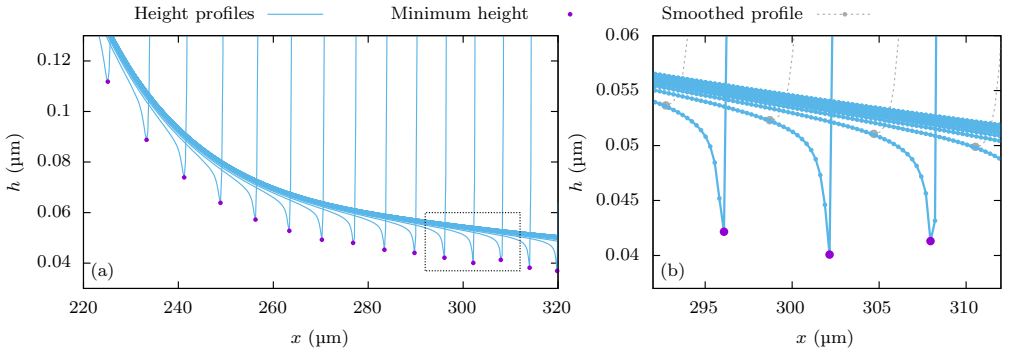

Figure 13: Zoomed-in plots of the height of the gas layer at intervals spaced 1.2009 µs apart for liquid viscosities of $\nu_l = 10\,\mathrm{mm}^2/\mathrm{s}$ using zero surface tension. All other parameters follow the baseline values in Table 2 and Table 3. Panel (a) shows the region marked by the dashed box in Figure 12(d). For each profile, the global minimum, which follows the leading tip, is also plotted on the curves. Panel (b) shows the region marked by the dashed box in panel (a). In panel (b), the small blue circles indicate the computational grid. The gray dashed lines show the profiles with Gaussian smoothing applied, and the gray circles show the global minima of the smoothed lines.

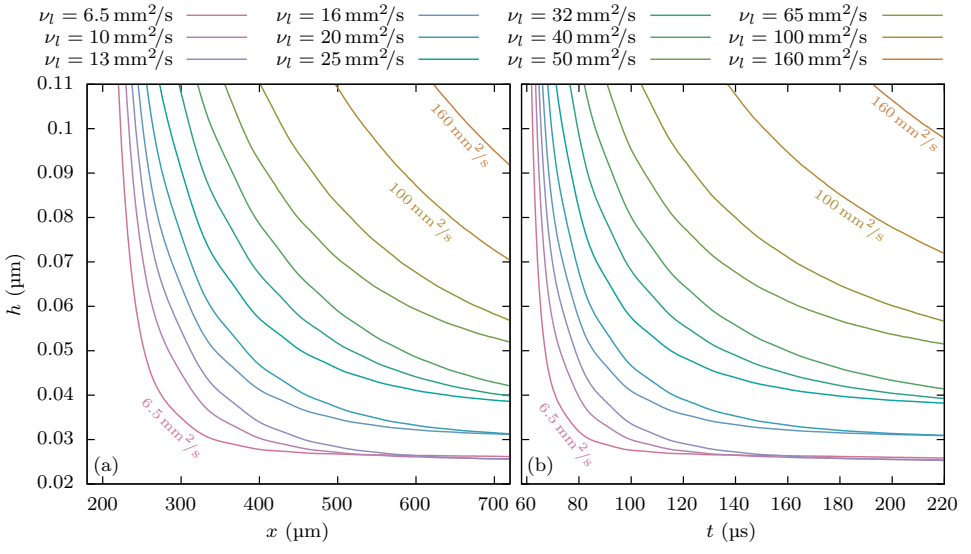

Figure 14: Trajectories of the global minimum of the drop profile in (a) the (x, h) plane, and (b) the (t, h) plane for a range of different liquid viscosities, using the baseline parameters in Table 2 and Table 3 and zero surface tension. Simulations with $13\,\mathrm{mm}^2/\mathrm{s} < \nu_l \leqslant 40\,\mathrm{mm}^2/\mathrm{s}$ use a grid of size 8192×1536, and simulations with $\nu_l \leqslant 13\,\mathrm{mm}^2/\mathrm{s}$ use a grid of size 12288×2304. Trajectories for selected ν_l are labeled.

in the thin gas layer. Lift-off appears to occur at $x \approx 280\,\mu\mathrm{m}$ and the leading tip starts to rise. However the influence of the capillary wave causes the tip to move downward again, ultimately dipping below the previous minimum height. It is possible that the tip may move upward again at a later point, but we were unable to track the behavior further. The sharp features visible in Figure 15(a) (e.g., at $(x, h) \approx (700\,\mu\mathrm{m}, 100\,\mu\mathrm{m})$) cause the simulation to terminate early, since

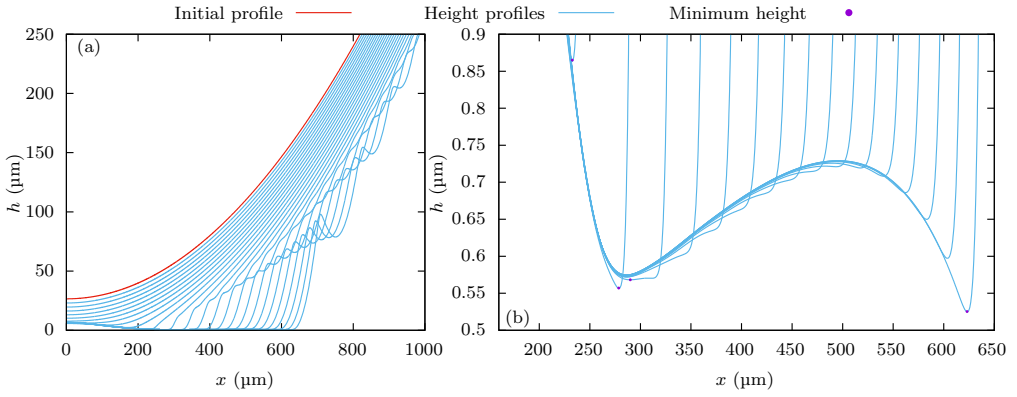

Figure 15: (a) Profiles of the height of the gas layer at intervals spaced 11.80 μs apart for a liquid viscosity of $\nu_l = 6.5\,\mathrm{mm}^2/\mathrm{s}$ and initial drop velocity of $V = 0.3\,\mathrm{m/s}$, showing the development of capillary waves. All other parameters use the baseline values in Table 2 and Table 3. (b) Zoomed-in plot of the same data. The global minima of the curves are plotted when they indicate the leading tip.

the Newton–Raphson iterations can no longer be solved to an acceptable level of accuracy.

4.4. *Effect of compressibility in the gas*

We performed simulations to examine the lift-off behavior in the regime of high initial drop velocity when compressibility in the gas becomes important. We chose $V = 2\,\mathrm{m/s}$, which is substantially into the compressible regime of Figure 3. We focused on $\nu_l = 32\,\mathrm{mm}^2/\mathrm{s}$, and due to the faster dynamics in the regime, we halved the timestep multiplier from its baseline value, to $\zeta = 4 \times 10^{-3}$. Figure 16(a) shows that the behavior is qualitatively different in this case, with the central dimple noticeably rebounding while the drop profile spreads outward. Figure 16(b) shows a zoomed-in region of the thin gas layer. Other than V, all physical simulation parameters are identical to those used in Figure 4(e), yet the results are considerably different with a much thinner gas layer, and visually, they are a closer match to the simulations without surface tension. For these simulations, we were therefore not able to identify the lift-off time. Figure 16(c) shows plots of the centerline height $h(0, t)$ for four different values of V indicating that the relative rebound of the central dimple is much larger for higher drop impact velocities.

5. Conclusion

In this paper we investigated the viscous effects in the early stages of drop impact on a surface. We coupled a Navier–Stokes solver to model flow in the interior of the drop with a partial differential equation to model the pressure and height in the thin gas layer between the drop and the surface. We demonstrated that our simulations are consistent with previous work using potential flow theory where flow in the liquid is assumed incompressible (Mandre *et al.* 2009; Mani *et al.* 2010; Mandre & Brenner 2012). However, our simulations allow us to go beyond this previous work and investigate viscous effects. We showed that at low initial drop velocities, viscosity plays a weak role in the deceleration of the drop, and the height H^* at which it reaches a stagnation point.

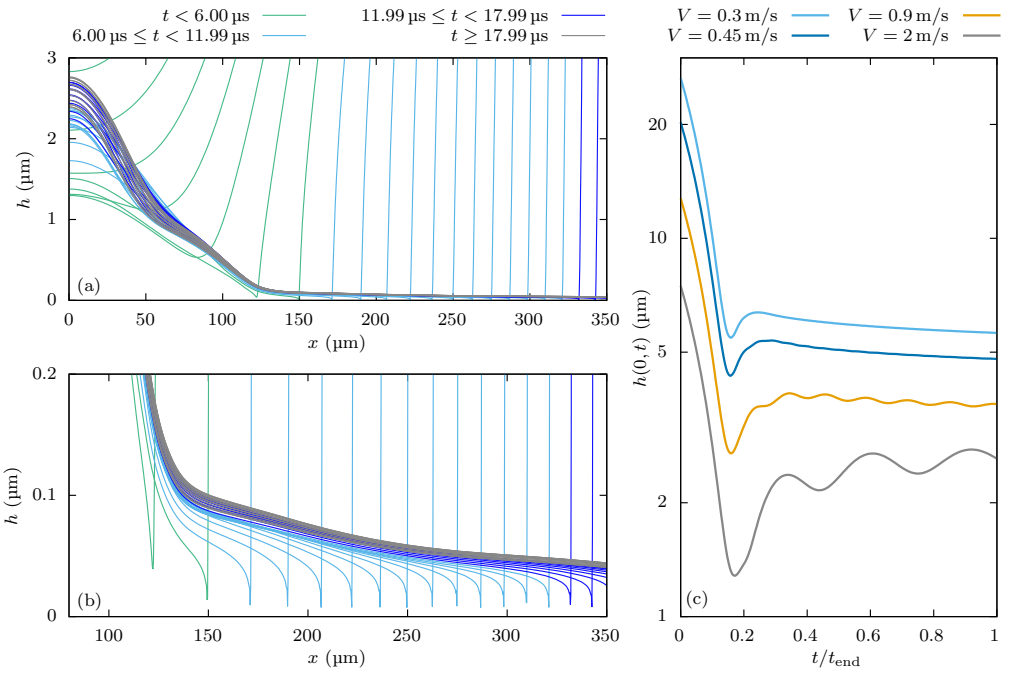

Figure 16: (a) Profiles of the height of the gas layer spaced 0.4998 μs apart for a liquid viscosity of $\nu_l = 32\,mm^2/s$ and an initial drop velocity of $V = 2\,m/s$, where the gas compressibility becomes important. The timestep multiplier is set to $\zeta = 4 \times 10^{-3}$. All other parameters use the baseline values in Table 2 and Table 3. (b) Zoomed-in plot of the same data. (c) Semi-log plot of the centerline height $h(0,t)$ for four different drop velocities when $\nu_l = 32\,mm^2/s$, with all other parameters using the baseline values.

Using our simulations, we are able to recreate the lift-off phenomenon that was experimentally reported by Kolinski *et al.* (2014*b*). We have therefore demonstrated that with the reduced model described in Section 2, our simulations are able to capture lift-off. Our numerical results for the lift-off time τ are consistent with the $\nu_l^{1/2}$ scaling relationship found by Kolinski *et al.* (2014*b*). However, the additional precision afforded by the simulations indicates that the precise relationship between τ and ν_l is more complex, due to the effects of capillary waves and the sensitivity of the results to the definition of the time origin. The simulation allows us to probe conditions that would be difficult to observe experimentally. Using this capability, our results provide strong evidence that surface tension is necessary for lift-off to occur. This is consistent with the numerical study of Duchemin & Josserand (2011), who found that surface tension was required for the formation of a thin jet skating above the surface. In their study, the absence of surface tension led to a finite-time singularity where the liquid–gas interface touches the substrate, whereas in our case the interface asympotically approaches the substrate. However, there are several differences between their simulations and ours, such as the usage of axisymmetric coordinates, and a different way to represent the liquid–gas interface and solve for the relevant physical variables. It is therefore difficult to make an exact comparison.

There are a number of possible next steps. The simulations provide a detailed view of the lift-off phenomenon, and all aspects (e.g., stress, velocity, vorticity)

can be calculated. The results may therefore guide theoretical analyses of lift-off, and may allow scaling relationships similar to those presented by Mandre *et al.* (2009); Mandre & Brenner (2012) and Mani *et al.* (2010) to be derived. As part of our study, we have released a complete high-performance open source code that can examine lift-off across a wide range of configurations.

We opted to use a fixed-grid simulation for simplicity in coupling the liquid domain and gas layer together, and as described in Appendices B and C we are able to obtain accurate simulation results in a reasonable timeframe. However, it is likely that the behavior at the bottom of the liquid domain, close to the liquid–gas interface and near the leading tip, dominates. Because of this, the simulation is a good candidate for use with adaptive mesh refinement (AMR) (Berger & Oliger 1984; Guittet *et al.* 2015), where the liquid–gas interface and the region around the leading tip could use a finer mesh. AMR has already been used for full-scale simulations of droplet impact, such as those using the Gerris/Basilisk software (Philippi *et al.* 2016; Popinet 2003, 2009; Lagrée *et al.* 2011; Popinet 2015), but it could also be a useful avenue to explore for our reduced model. It would result in substantial computational savings, although the liquid–gas coupling would become more complicated and numerical errors would be harder to quantify.

The simulation could also be generalized to use cylindrical axisymmetric coordinates. The overall numerical approach would stay the same, but additional radial factors would have to be incorporated throughout the simulation. The Navier–Stokes solver that we employ has already been demonstrated to work in axisymmetric coordinates (Yu *et al.* 2003, 2007), but the routines that involve the gas layer would require modifications. For example, the kernel in equation (2.10) would need to be modified. While the current simulation is already in good agreement with the experimental results of Kolinski *et al.* (2014*b*), an axisymmetric solver would allow for a near-perfect comparison. This would, for example, help elucidate further the precise relationship between lift-off time τ and liquid viscosity ν_l.

Experiments by Thoroddsen and coworkers have used interferometry to examine the evolution of the gas layer across a full two-dimensional surface (Langley *et al.* 2017). Their results show a number of interesting effects beyond the scope of our current model, such as a breakage of rotational symmetry and the formation of ruptures in the air film (Langley *et al.* 2017; Li *et al.* 2017). They have also examined the case of nano-rough surfaces (Langley *et al.* 2018). To connect with this work, our model could be generalized to a full three-dimensional simulation of the liquid and two-dimensional simulation of the gas layer. This would be substantially more computationally challenging, and would be a good candidate for using parallel computing and adaptive mesh refinement (Zhang *et al.* 2019).

Funding. C. H. R. was partially supported by the National Science Foundation under Grant No. DMS-1753203. C. H. R. was partially supported by the Applied Mathematics Program of the U.S. DOE Office of Science Advanced Scientific Computing Research under Contract No. DE-AC02-05CH11231.

Declaration of interests. The authors report no conflict of interest.

Data availability statement. The C++ code to generate all of these results is provided in the GitHub repository at `https://github.com/chr1shr/vdropimpact`. The code makes use of the TGMG library, which is provided in a separate GitHub repository at `https://github.com/chr1shr/tgmg`.

Author ORCID. C. H. Rycroft, https://orcid.org/0000-0003-4677-6990; S. Mishra, https://orcid.org/0000-0002-9487-5531; S. M. Rubinstein, https://orcid.org/0000-0002-2897-2579

Appendix A. Calculations for the governing equation in the gas layer

A.1. *Derivation of the gas layer pressure update equation*

Substituting for ρ_g from the equation of state, equation (2.5), into the lubrication equation for the pressure in the gas layer, equation (2.4), we get

$$12\mu_g \left(\left(\frac{\rho_0}{p_0^{1/\gamma}} p_g^{1/\gamma} \right) h \right)_t = \left(\left(\frac{\rho_0}{p_0^{1/\gamma}} p_g^{1/\gamma} \right) h^3 p_{g,x} \right)_x . \tag{A 1}$$

Dividing both sides by $\rho_0 / p_0^{1/\gamma}$,

$$12\mu_g \left(p_g^{1/\gamma} h \right)_t = \left(p_g^{1/\gamma} h^3 p_{g,x} \right)_x . \tag{A 2}$$

Using the product rule to expand the brackets,

$$12\mu_g \left(\frac{1}{\gamma} p_g^{1/\gamma - 1} p_{g,t} h + p_g^{1/\gamma} h_t \right) = \frac{1}{\gamma} p_g^{1/\gamma - 1} p_{g,x} h^3 p_{g,x} + p_g^{1/\gamma} 3h^2 h_x p_{g,x} + p_g^{1/\gamma} h^3 p_{g,xx}. \tag{A 3}$$

Dividing both sides by $p_g^{1/\gamma - 1}$,

$$12\mu \left(\frac{1}{\gamma} p_{g,t} h + p_g h_t \right) = \frac{1}{\gamma} p_{g,x} h^3 p_{g,x} + p_g 3h^2 h_x p_{g,x} + p_g h^3 p_{g,xx}. \tag{A 4}$$

Dropping the subscript g for gas yields

$$12\mu \left(\frac{1}{\gamma} p_t h + p h_t \right) = \frac{1}{\gamma} p_x h^3 p_x + p 3h^2 h_x p_x + p h^3 p_{xx}, \tag{A 5}$$

which can be rearranged to give equation (3.4).

A.2. *Numerical solution of the gas layer pressure*

We now describe how to solve equation (3.5) in the main text for updating the gas layer pressure using the Newton–Raphson method. Let P^k be a vector containing the pressure estimates at the kth Newton–Raphson iteration. As an initial estimate, we set P^0 to be the pressure values from the nth timestep. We then write (3.5) as a nonlinear system $F(P) = 0$, where the ith component of F is given by the (L.H.S. − R.H.S.) of equation (3.5) evaluated at the ith gridpoint. An improved estimate P^{k+1} for the pressure is given in terms of P^k by

$$J_F(P^k) \left(P^{k+1} - P^k \right) = -F(P^k), \tag{A 6}$$

where $J_F(P^k)$ is the Jacobian of F, which has components

$$J_{F,ij}^{k+1} = \frac{\partial F_i}{\partial P_j^{k+1}}. \tag{A 7}$$

Since the finite-difference stencils in equation (3.5) only involve adjacent grid points, J_F is a tridiagonal system. It can be written as

$$J_F = \begin{pmatrix} b_0 & c_0 & & & \\ a_1 & b_1 & c_1 & & \\ & a_2 & b_2 & c_2 & \\ & & \ddots & \ddots & \ddots \end{pmatrix}, \tag{A 8}$$

where the terms are given by

$$a_i = \frac{\partial F}{\partial p_{i-1}^{n+1}} = \frac{1}{\gamma}\frac{\bar{h}^3}{\Delta x}\left(\frac{p_{i+1}^{n+1} - p_{i-1}^{n+1}}{2\Delta x}\right) - \frac{3\bar{h}^2\bar{h}_x}{2\Delta x}p_i^{n+1} + \frac{\bar{h}^3}{\Delta x^2}p_i^{n+1}, \tag{A 9}$$

$$b_i = \frac{\partial F}{\partial p_i^{n+1}} = -12\frac{\mu}{\gamma}\frac{\bar{h}}{\Delta t}(1) - 12\mu\bar{h}_t - \left[\frac{3\bar{h}^2\bar{h}_x}{2\Delta x}\left(p_{i+1}^{n+1} - p_{i-1}^{n+1}\right) + \frac{\bar{h}^3}{\Delta x^2}\left(p_{i+1}^{n+1} - 2p_i^{n+1} + p_{i-1}^{n+1}\right) + \frac{\bar{h}^3}{\Delta x^2}p_i^{n+1}(-2)\right], \tag{A 10}$$

$$c_i = \frac{\partial F}{\partial p_{i+1}^{n+1}} = -\frac{1}{\gamma}\frac{\bar{h}^3}{\Delta x}\left(\frac{p_{i+1}^{n+1} - p_{i-1}^{n+1}}{2\Delta x}\right) - \frac{3\bar{h}^2\bar{h}_x}{2\Delta x}p_i^{n+1} - \frac{\bar{h}^3}{\Delta x^2}p_i^{n+1}. \tag{A 11}$$

Solving equation (A 6) can be done efficiently using LAPACK's tridiagonal solver `dgtsv` (Anderson *et al.* 1999). In most cases, since the pressure does not change by a large amount per timestep, fewer than five iterations are required in order to achieve numerical convergence.

Appendix B. Tests of the simulation performance

Table 4 contains statistics about the performance of the code for several simulations that were referenced in the main text. All tests were run using ten threads on an Ubuntu Linux computer with a ten-core 2.8 GHz Intel Core i9-10900 CPU, and the code was compiled with GCC version 10.3.

The initial dynamics simulations only need to capture the large-scale deformation of the drop, and can therefore be run on relatively coarse computational grids. Consequently, a typical simulation takes approximately 40 min of wall clock time to run. A large portion of the computation time is spent on solving the linear systems with the multigrid method. This should be expected since the multigrid V-cycles involve repeated scans over the entire grid. Collectively, the four multigrid solves take up 44% of the total computation time. The MAC and FEM linear systems take slightly more time and V-cycles, since apart from where Dirichlet boundary conditions are applied, these linear systems are only weakly diagonally dominant. By contrast, the linear systems for the implicit viscous term are strictly diagonally dominant. We note that the linear systems for the u and v velocity components are slightly different, since at $x = 0$ we apply different boundary conditions, $(u, v_x) = (0, 0)$. Hence it is not possible to vectorize this system, and there is no substantial computational advantage over solving for the updates to u and v separately.

Calculating the boundary conditions according to equation (2.10) requires applying Simpson's rule along the M gridpoints on the bottom edge. This must be done for the top edge of length M, and the right edge of length N, requiring

	Initial dynamics, $\nu_l = 10\,\mathrm{mm}^2/\mathrm{s}$	Lift-off, $\nu_l = 10\,\mathrm{mm}^2/\mathrm{s}$	Lift-off, $\nu_l = 100\,\mathrm{mm}^2/\mathrm{s}$
Grid size	2048×256	5120×960	5120×960
Total WC time	0.641 h	20.6 h	29.8 h
Total timesteps	28500	71250	95000
WC time / timestep	81 ms	1041 ms	1130 ms
WC fraction on gas layer	0.25%	0.047%	0.045%
WC fraction on BCs	3.39%	1.61%	1.49%
WC fraction on MAC solve	11.21%	13.05%	12.09%
WC fraction on FEM solve	12.77%	14.31%	14.36%
WC fraction on viscous solve	20.11%	26.67%	31.12%
Mean MAC V-cycles	5	4.4	4.5
Mean FEM V-cycles	5.6	4.9	5.3
Mean viscosity V-cycles	3.7	4.3	5.5

Table 4: Performance statistics for several different simulations, compiled using GCC 10.3 on an Ubuntu Linux computer with an 2.8 GHz Intel Core i9-10900 CPU. Ten threads were used, and all simulations use the baseline parameter choices in Table 2 & 3 unless otherwise noted. The wall clock (WC) time is reported for each test, and the fraction of time on major components, such as the computation of boundary conditions (BCs), solving the marker-and-cell (MAC) linear system, and solving finite-element method (FEM) linear system, are reported.

$\mathcal{O}(M(M+N))$ work in total. This is sizable amount of work and takes 3.4% of the total computation time. Even though the gas layer involves several Newton steps and tridiagonal matrix solves, it only needs $\mathcal{O}(M)$ work and therefore takes up a minimal amount of the total computation time.

Table 4 also contains performance information for two lift-off simulations, which are run on larger computational grids to obtain high accuracy in the height of the gas layer. The wall clock time per timestep increases from 81 ms to 1.041 s. Based on a linear scaling with gridpoints, we would expect 81 ms to increase to $(81\text{ ms})\frac{5120\times960}{2048\times256} = 760$ ms. Thus the performance is comparable, but slightly worse than, linear scaling, which may be due to reduced cache efficiency for a larger grid. Overall, the percentages spent on the different parts of the simulation are comparable, although the fraction spent on multigrid V-cycles increases slightly, and the fraction spent on the gas layer (which scales like $\mathcal{O}(M)$) decreases. In particular, more V-cycles are required to handle the implicit viscosity linear system when ν_l is larger.

Appendix C. Tests of the simulation accuracy

The simulation domain size, which is set via the non-dimensional parameter $\tilde{L}$ in Table 3 and the domain aspect ratio β, may have an effect on the results. Since the boundary conditions on the top and right boundaries are based on an inviscid assumption, the domain size affects the extent to which viscosity is resolved. In addition, when solving for the pressure in the gas layer, the boundary condition of $p = P_0$ is imposed at $x = L$, and thus extending the domain affects the influence of this boundary condition on the simulation.

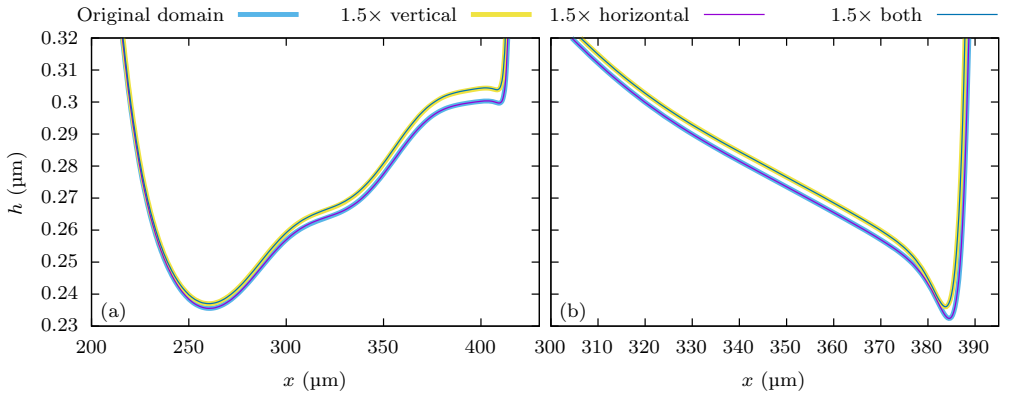

Figure 17: Plots of the height profiles at $t = 102.07\,\mu s$ for simulations with (a) liquid viscosity $\nu_l = 10\,mm^2/s$ and (b) liquid viscosity $\nu_l = 100\,mm^2/s$. Baseline parameters from Table 2 & Table 3 are used although the original domain size for both values of ν_l uses $\tilde{L} = 30$ and $\beta = 16/3$. Results are also shown where the simulation domain is extended by a factor of 1.5 in either or both dimensions. In the extended simulations, the number of grid points is increased to keep the grid spacings $\Delta x = \Delta y$ the same.

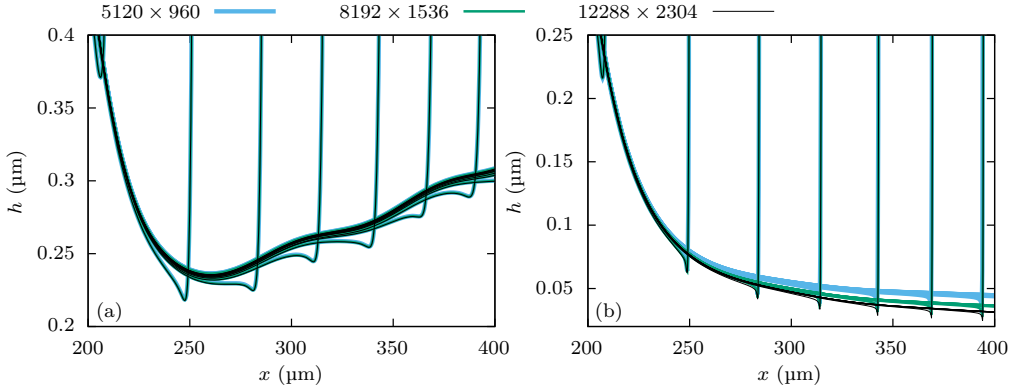

Figure 18: Plots of the height profiles spaced 6.004 µs apart for three different resolutions using the baseline parameters from Table 2 & Table 3, and liquid viscosity $\nu_l = 10\,mm^2/s$, with (a) surface tension $\sigma = 0.072\,N/m$, and (b) zero surface tension.

To test the sensitivity of the simulation results to the domain size, we performed simulations where either the horizontal dimension, vertical dimension, or both dimensions were extended by a factor of 1.5. In each of these simulations the grid spacings $\Delta x = \Delta y$ were kept the same, so that the horizontal extension increases the grid points from 5120 to 7680, and the vertical extension increases the grid points from 960 to 1440. Figure 17 shows the height profiles in the thin gas layer for the four simulations, for (a) $\nu_l = 10\,mm^2/s$ and (b) $\nu_l = 100\,mm^2/s$. The vertical extensions give visually indistinguishable curves, indicating that the vertical dimension is sufficiently large to resolve the viscous effects even for the larger value of ν_l. The horizontal extensions create minor vertical shifts in the curves, suggesting that the pressure boundary condition has an effect on the results. However, these shifts are still acceptably small, and result in no substantial change to the position and time at which lift-off occurs.

We also examined the sensitivity of the results to the numerical grid size. Figure 18(a) shows height profiles for a simulation using the baseline parameters with liquid viscosity $\nu_l = 10\,\mathrm{mm}^2/\mathrm{s}$ and surface tension $\sigma = 0.072\,\mathrm{N/m}$. Simulations with higher resolutions of 8192×1536 and 12288×2304 are also plotted, resulting in visually indistinguishable results. Figure 18(b) shows height profiles when the surface tension is set to zero and all other parameters are kept the same. In this case, as discussed in Section 4.3, the leading tip becomes very sharp since the regularizing effect of surface tension is removed. As the tip moves across the grid, there will be a resolution-dependent numerical diffusion that will act as an effective small surface tension. Thus in this case there is a small shift in the height profiles. While this remains small, it makes the precise behavior of the leading tip difficult to resolve for small values of ν_l, requiring larger grid sizes as presented in Section 4.3.

REFERENCES

Almgren, Ann S., Bell, John B., Colella, Phillip, Howell, Louis H. & Welcome, Michael L. 1998 A Conservative Adaptive Projection Method for the Variable Density Incompressible Navier–Stokes Equations. *Journal of Computational Physics* **142** (1), 1–46.

Almgren, Ann S., Bell, John B. & Szymczak, William G. 1996 A Numerical Method for the Incompressible Navier–Stokes Equations Based on an Approximate Projection. *SIAM Journal on Scientific Computing* **17** (2), 358–369.

Anderson, E., Bai, Z., Bischof, C., Blackford, S., Demmel, J., Dongarra, J., Du Croz, J., Greenbaum, A., Hammarling, S., McKenney, A. & Sorensen, D. 1999 *LAPACK Users' Guide*, 3rd edn. Philadelphia, PA: Society for Industrial and Applied Mathematics.

Bell, John B., Colella, Phillip & Glaz, Harland M. 1989 A second-order projection method for the incompressible Navier–Stokes equations. *Journal of Computational Physics* **85** (2), 257–283.

Bell, John B., Howell, Louis H. & Colella, Phillip 1991 An efficient second-order projection method for viscous incompressible flow. In *10th Computational Fluid Dynamics Conference*, p. 360.

Berger, Marsha J. & Oliger, Joseph 1984 Adaptive mesh refinement for hyperbolic partial differential equations. *Journal of Computational Physics* **53** (3), 484–512.

Boelens, Arnout M. P. & de Pablo, Juan J. 2018 Simulations of splashing high and low viscosity droplets. *Physics of Fluids* **30** (7), 072106.

Byrd, Richard H., Lu, Peihuang, Nocedal, Jorge & Zhu, Ciyou 1995 A Limited Memory Algorithm for Bound Constrained Optimization. *SIAM Journal on Scientific Computing* **16** (5), 1190–1208.

Chorin, Alexandre J. 1967 A numerical method for solving incompressible viscous flow problems. *Journal of Computational Physics* **2** (1), 12–26.

Chorin, Alexandre J. 1968 Numerical Solution of the Navier–Stokes Equations. *Mathematics of Computation* **22** (104), 745–762.

Colella, Phillip 1985 A Direct Eulerian MUSCL scheme for gas dynamics. *SIAM Journal on Scientific and Statistical Computing* **6** (1), 104–107.

Colella, Phillip 1990 Multidimensional upwind methods for hyperbolic conservation laws. *Journal of Computational Physics* **87** (1), 171–200.

Courant, Richard, Friedrichs, Kurt & Lewy, Hans 1967 On the Partial Difference Equations of Mathematical Physics. *IBM Journal of Research and Development* **11** (2), 215–234.

Driscoll, Michelle M. & Nagel, Sidney R. 2011 Ultrafast Interference Imaging of Air in Splashing Dynamics. *Phys. Rev. Lett.* **107**, 154502.

Driscoll, Michelle M., Stevens, Cacey S. & Nagel, Sidney R. 2010 Thin film formation during splashing of viscous liquids. *Phys. Rev. E* **82**, 036302.

Duchemin, Laurent & Josserand, Christophe 2011 Curvature singularity and film-skating during drop impact. *Physics of Fluids* **23** (9), 091701.

Duchemin, Laurent & Josserand, Christophe 2020 Dimple drainage before the coalescence of a droplet deposited on a smooth substrate. *Proceedings of the National Academy of Sciences* **117** (34), 20416–20422.

Eggers, Jens, Fontelos, Marco A., Josserand, Christophe & Zaleski, Stéphane 2010 Drop dynamics after impact on a solid wall: Theory and simulations. *Physics of Fluids* **22** (6), 062101.

Guittet, Arthur, Theillard, Maxime & Gibou, Frédéric 2015 A stable projection method for the incompressible Navier–Stokes equations on arbitrary geometries and adaptive Quad/Octrees. *Journal of Computational Physics* **292**, 215–238.

Heath, Michael T. 2002 *Scientific Computing: An Introductory Survey*. McGraw-Hill.

Hicks, Peter D. & Purvis, Richard 2010 Air cushioning and bubble entrapment in three-dimensional droplet impacts. *Journal of Fluid Mechanics* **649**, 135–163.

Jian, Zhen, Josserand, Christophe, Popinet, Stéphane, Ray, Pascal & Zaleski, Stéphane 2018 Two mechanisms of droplet splashing on a solid substrate. *Journal of Fluid Mechanics* **835**, 1065–1086.

Josserand, Christophe & Thoroddsen, Sigurdur T. 2016 Drop impact on a solid surface. *Annual Review of Fluid Mechanics* **48**, 365–391.

Josserand, Christophe & Zaleski, Stéphane 2003 Droplet splashing on a thin liquid film. *Physics of Fluids* **15** (6), 1650–1657.

Kolinski, John M, Kaviani, Ramin, Hade, Dylan & Rubinstein, Shmuel M 2019 Surfing the capillary wave: wetting dynamics beneath an impacting drop. *Physical Review Fluids* **4** (12), 123605.

Kolinski, John M., Mahadevan, L. & Rubinstein, Shmuel M. 2014*a* Drops can bounce from perfectly hydrophilic surfaces. *EPL (Europhysics Letters)* **108** (2), 24001.

Kolinski, John M, Mahadevan, L. & Rubinstein, Shmuel M. 2014*b* Lift-off instability during the impact of a drop on a solid surface. *Physical Review Letters* **112** (13), 134501.

Kolinski, John M., Rubinstein, Shmuel M., Mandre, Shreyas, Brenner, Michael P., Weitz, David A. & Mahadevan, L. 2012 Skating on a film of air: drops impacting on a surface. *Physical Review Letters* **108** (7), 074503.

Lagrée, P-Y, Staron, Lydie & Popinet, Stéphane 2011 The granular column collapse as a continuum: validity of a two-dimensional Navier–Stokes model with a μ (I)-rheology. *Journal of Fluid Mechanics* **686**, 378–408.

Langley, Kenneth, Li, Er Qiang & Thoroddsen, Sigurdur T. 2017 Impact of ultra-viscous drops: air-film gliding and extreme wetting. *Journal of Fluid Mechanics* **813**, 647–666.

Langley, Kenneth R., Li, Er Qiang, Vakarelski, Ivan U. & Thoroddsen, Sigurdur T. 2018 The air entrapment under a drop impacting on a nano-rough surface. *Soft Matter* **14**, 7586–7596.

Latka, Andrzej, Strandburg-Peshkin, Ariana, Driscoll, Michelle M., Stevens, Cacey S. & Nagel, Sidney R. 2012 Creation of Prompt and Thin-Sheet Splashing by Varying Surface Roughness or Increasing Air Pressure. *Phys. Rev. Lett.* **109**, 054501.

Li, Er Qiang, Langley, Kenneth R., Tian, Yuan Si, Hicks, Peter D. & Thoroddsen, Sigurdur T. 2017 Double Contact During Drop Impact on a Solid Under Reduced Air Pressure. *Physical Review Letters* **119**, 214502.

Mandre, Shreyas & Brenner, Michael P. 2012 The mechanism of a splash on a dry solid surface. *Journal of Fluid Mechanics* **690**, 148–172.

Mandre, Shreyas, Mani, Madhav & Brenner, Michael P. 2009 Precursors to splashing of liquid droplets on a solid surface. *Physical Review Letters* **102** (13), 134502.

Mani, Madhav, Mandre, Shreyas & Brenner, Michael P. 2010 Events before droplet splashing on a solid surface. *Journal of Fluid Mechanics* **647**, 163–185.

Moore, M. R., Ockendon, J. R. & Oliver, J. M. 2013 Air-cushioning in impact problems. *IMA Journal of Applied Mathematics* **78** (4), 818–838.

Pasandideh-Fard, M., Qiao, Y. M., Chandra, Sanjeev & Mostaghimi, Javad 1996 Capillary effects during droplet impact on a solid surface. *Physics of Fluids* **8** (3), 650–659.

Philippi, Julien, Lagrée, Pierre-Yves & Antkowiak, Arnaud 2016 Drop impact on a solid surface: short-time self-similarity. *Journal of Fluid Mechanics* **795**, 96–135.

Popinet, Stéphane 2003 Gerris: a tree-based adaptive solver for the incompressible Euler equations in complex geometries. *Journal of computational physics* **190** (2), 572–600.

Popinet, Stéphane 2009 An accurate adaptive solver for surface-tension-driven interfacial flows. *Journal of Computational Physics* **228** (16), 5838–5866.

Popinet, Stéphane 2015 A quadtree-adaptive multigrid solver for the Serre–Green–Naghdi equations. *Journal of Computational Physics* **302**, 336–358.

Range, Kai & Feuillebois, François 1998 Influence of surface roughness on liquid drop impact. *Journal of Colloid and Interface Science* **203** (1), 16–30.

Rein, Martin 1993 Phenomena of liquid drop impact on solid and liquid surfaces. *Fluid Dynamics Research* **12** (2), 61.

Renardy, Y., Popinet, S., Duchemin, L., Renardy, M., Zaleski, S., Josserand, C., Drumright-Clarke, M. A., Richard, D., Clanet, C. & Quéré, D. 2003 Pyramidal and toroidal water drops after impact on a solid surface. *Journal of Fluid Mechanics* **484**, 69–83.

Riboux, Guillaume & Gordillo, José Manuel 2014 Experiments of Drops Impacting a Smooth Solid Surface: A Model of the Critical Impact Speed for Drop Splashing. *Physical Review Letters* **113**, 024507.

Rioboo, R., Bauthier, C., Conti, J., Voue, M. & De Coninck, J. 2003 Experimental investigation of splash and crown formation during single drop impact on wetted surfaces. *Experiments in Fluids* **35** (6), 648–652.

Rioboo, R., Marengo, M. & Tropea, C. 2002 Time evolution of liquid drop impact onto solid, dry surfaces. *Experiments in Fluids* **33** (1), 112–124.

de Ruiter, Jolet, Oh, Jung Min, van den Ende, Dirk & Mugele, Frieder 2012 Dynamics of collapse of air films in drop impact. *Physical Review Letters* **108** (7), 074505.

Rycroft, Chris H., Wu, Chen-Hung, Yu, Yue & Kamrin, Ken 2020 Reference map technique for incompressible fluid–structure interaction. *Journal of Fluid Mechanics* **898**, A9.

Sprittles, James E. 2015 Air entrainment in dynamic wetting: Knudsen effects and the influence of ambient air pressure. *Journal of Fluid Mechanics* **769**, 444–481.

Stevens, Cacey S., Latka, Andrzej & Nagel, Sidney R. 2014 Comparison of splashing in high- and low-viscosity liquids. *Phys. Rev. E* **89**, 063006.

Sussman, Mark, Almgren, Ann S., Bell, John B., Colella, Phillip, Howell, Louis H. & Welcome, Michael L. 1999 An Adaptive Level Set Approach for Incompressible Two-Phase Flows. *Journal of Computational Physics* **148** (1), 81–124.

Taylor, Geoffrey & Saffman, P. G. 1957 Effects of Compressibility at Low Reynolds Number. *Journal of the Aeronautical Sciences* **24** (8), 553–562.

Thoroddsen, S. T., Etoh, T. G., Takehara, K., Ootsuka, N. & Hatsuki, Y. 2005 The air bubble entrapped under a drop impacting on a solid surface. *Journal of Fluid Mechanics* **545**, 203–212.

van der Veen, Roeland CA, Tran, Tuan, Lohse, Detlef & Sun, Chao 2012 Direct measurements of air layer profiles under impacting droplets using high-speed color interferometry. *Physical Review E* **85** (2), 026315.

Worthington, Arthur Mason 1877 XXVIII. On the forms assumed by drops of liquids falling vertically on a horizontal plate. *Proceedings of the Royal Society of London* **25** (171–178), 261–272.

Xu, Lei, Zhang, Wendy W. & Nagel, Sidney R. 2005 Drop splashing on a dry smooth surface. *Physical Review Letters* **94** (18), 184505.

Yarin, Alexander L. 2006 Drop impact dynamics: splashing, spreading, receding, bouncing.... *Annu. Rev. Fluid Mech.* **38**, 159–192.

Yu, Jiun-Der, Sakai, Shinri & Sethian, James A 2003 A coupled level set projection method applied to ink jet simulation. *Interfaces and Free Boundaries* **5** (4), 459–482.

Yu, Jiun-Der, Sakai, Shinri & Sethian, James A. 2007 Two-phase viscoelastic jetting. *Journal of Computational Physics* **220** (2), 568–585.

Zhang, Weiqun, Almgren, Ann, Beckner, Vince, Bell, John, Blaschke, Johannes, Chan, Cy, Day, Marcus, Friesen, Brian, Gott, Kevin, Graves, Daniel, Katz, Max P., Myers, Andrew, Nguyen, Tan, Nonaka, Andrew, Rosso, Michele, Williams, Samuel & Zingale, Michael 2019 AMReX: a framework for block-structured adaptive mesh refinement. *Journal of Open Source Software* **4** (37), 1370.